

# *Intraseasonal soil moisture-atmosphere feedbacks on the Tibetan Plateau circulation*

Article

Accepted Version

Talib, J., Taylor, C.M., Duan, A. and Turner, A. ORCID:  
<https://orcid.org/0000-0002-0642-6876> (2021) Intraseasonal  
soil moisture-atmosphere feedbacks on the Tibetan Plateau  
circulation. *Journal of Climate*, 34 (5). pp. 1789-1807. ISSN  
1520-0442 doi: 10.1175/JCLI-D-20-0377.1 Available at  
<https://centaur.reading.ac.uk/90790/>

It is advisable to refer to the publisher's version if you intend to cite from the  
work. See [Guidance on citing](#).

To link to this article DOI: <http://dx.doi.org/10.1175/JCLI-D-20-0377.1>

Publisher: American Meteorological Society

All outputs in CentAUR are protected by Intellectual Property Rights law,  
including copyright law. Copyright and IPR is retained by the creators or other  
copyright holders. Terms and conditions for use of this material are defined in  
the [End User Agreement](#).

[www.reading.ac.uk/centaur](http://www.reading.ac.uk/centaur)

**CentAUR**

Central Archive at the University of Reading

Reading's research outputs online

1     **Intraseasonal soil moisture-atmosphere feedbacks on the Tibetan Plateau**  
2                                     **circulation**

3                                     Joshua Talib \*

4                                     *UK Centre for Ecology and Hydrology, Wallingford, UK*

5                                     Christopher M. Taylor

6                                     *UK Centre for Ecology and Hydrology and National Centre for Earth Observation, Wallingford,*  
7                                     *UK*

8                                     Anmin Duan

9                                     *State Key Laboratory of Numerical Modelling for Atmospheric Sciences and Geophysical Fluid*  
10                                    *Dynamics, Institute of Atmospheric Physics, Chinese Academy of Science (CAS), Beijing 100029,*  
11                                    *China*

12                                    Andrew G. Turner

13                                    *Department of Meteorology, University of Reading, UK and National Centre for Atmospheric*  
14                                    *Science, University of Reading, UK*

15    \* *Corresponding author address:* UK Centre for Ecology and Hydrology, Wallingford, UK

16    E-mail: jostal@ceh.ac.uk

## ABSTRACT

17 Substantial intraseasonal precipitation variability is observed across the Ti-  
18 betan Plateau (TP) during boreal summer associated with the subtropical jet  
19 location and the Silk Road pattern. Weather station data and satellite obser-  
20 vations highlight a sensitivity of soil moisture and surface fluxes to this vari-  
21 ability. During rain-free periods of two or more days, skin temperatures are  
22 shown to rise as the surface dries, signalling decreased evaporative fraction.  
23 Surface fluxes are further enhanced by relatively clear skies. In this study we  
24 use an atmospheric reanalysis to assess how this surface flux response across  
25 the TP influences local and remote conditions.

26 Increased surface sensible heat flux induced by decreased soil moisture dur-  
27 ing a regional dry event leads to a deepening of the planetary boundary-layer  
28 and the development of a heat low. Consistent with previous studies, heat  
29 low characteristics exhibit pronounced diurnal variability driven by anoma-  
30 lous daytime surface warming. For example, low-level horizontal winds are  
31 weakest during the afternoon and intensify overnight when boundary-layer  
32 turbulence is minimal. The heat low favours an upper-tropospheric anticy-  
33 clone which induces an upper-level Rossby wave and leads to negative upper-  
34 level temperature anomalies across southern China. The Rossby wave inten-  
35 sifies the upper-level cyclonic circulation across central China, whilst upper-  
36 level negative temperature anomalies across south China extends the west Pa-  
37 cific subtropical high westward. These circulation anomalies influence tem-  
38 perature and precipitation anomalies across much of China. The association  
39 between land-atmosphere interactions across the TP, large-scale atmospheric  
40 circulation characteristics, and precipitation in east Asia highlights the impor-  
41 tance of intraseasonal soil moisture dynamics on the TP.

## 42 **1. Introduction**

43 With an average height of 4500m and an area of approximately 2.5 million km<sup>2</sup>, dynamic and  
44 thermodynamic processes over the Tibetan Plateau (TP, shown in Fig. 1a at approximately 28 to  
45 40°N and 80 to 105°E) influence the large-scale atmospheric circulation across Eurasia. The TP  
46 surface provides a mid-tropospheric heat source in the mid-latitudes that opposes the textbook  
47 view of the zonal-mean Hadley circulation, intensifies the Indian and East Asian monsoons  
48 (Kutzbach et al. 1993; Molnar et al. 1993; Zhisheng et al. 2001; Duan and Wu 2005; Jiang  
49 et al. 2008), and varies the East Asian subtropical front location (Jiang et al. 2008; Wang et al.  
50 2008; Liu et al. 2012; Wang et al. 2014). Substantial efforts have taken place to understand the  
51 sensitivity of interannual precipitation variability to TP land surface warming (Li and Yanai 1996;  
52 Duan and Wu 2005; Liu et al. 2012; Wang et al. 2014). However, there has been less attention  
53 paid to the impact of intraseasonal TP surface warming on atmospheric conditions.

54 Surface sensible heat flux (SHF) is controlled by incoming radiation, temperature, humidity,  
55 low-level wind, and land surface characteristics. Certain land surface properties such as veg-  
56 etation cover, leaf area, and aerodynamic roughness change relatively slowly over the season.  
57 Meanwhile soil moisture, particularly near the surface, fluctuates strongly in response to rainfall,  
58 and decreases more gradually during dry spells. When vegetation is sparse, surface fluxes are  
59 sensitive to soil moisture due to substantial variations in evaporation. A recent observational study  
60 at a weather station located in a semi-arid region that extends across the central TP highlights  
61 that sub-seasonal variations in evaporation are predominately due to changes in soil evaporation  
62 rather than plant transpiration (Cui et al. 2020). Favouring of surface SHF over surface latent  
63 heat flux (LHF) during periods of soil moisture deficiency increases near-surface air temperatures  
64 (Koster et al. 2009; Miralles et al. 2012; Berg et al. 2014; Schwingshackl et al. 2017) and impacts

65 boundary-layer and large-scale circulation characteristics (Notaro and Zarrin 2011; Xue et al.  
66 2012; Wan et al. 2017). Variations in surface fluxes also influence the intensity of drought and  
67 heatwave events (Zampieri et al. 2009; Weisheimer et al. 2011; Loikith and Broccoli 2012;  
68 Quesada et al. 2012; Chiriaco et al. 2014; Schumacher et al. 2019). In this study the sensitivity  
69 of surface fluxes and the atmospheric circulation to intraseasonal precipitation and soil moisture  
70 variability across the TP is investigated. In particular the influence of soil moisture deficiency  
71 across the TP on the development of heat lows and remote atmospheric conditions is explored.

72 Numerous observational and modelling studies demonstrate a sensitivity of local and remote  
73 atmospheric conditions to land surface characteristics on intraseasonal to interannual timescales.  
74 For example, interannual boreal summer rainfall variability across southern North America  
75 (Carleton et al. 1990) is associated with land surface characteristics across mountainous regions  
76 in western North America (Gutzler 2000; Lo and Clark 2002; Hu and Feng 2004; Notaro and  
77 Zarrin 2011; Xue et al. 2012, 2016, 2018; Diallo et al. 2019). Anomalously deep snowpack  
78 across high terrain regions in western North America increases surface albedo and provides a  
79 more persistent soil moisture source associated with decreased lower-tropospheric temperatures,  
80 a reduced land-ocean thermal gradient, a delayed poleward migration of the North American  
81 monsoon, and negative rainfall anomalies across southwest North America (Gutzler 2000; Lo  
82 and Clark 2002; Notaro and Zarrin 2011). There is also a significant relationship between late  
83 spring land surface temperature anomalies across western North America and boreal summer  
84 precipitation over the Southern Great Plains (Xue et al. 2012, 2016, 2018; Diallo et al. 2019). A  
85 positive land surface temperature anomaly across western North America increases surface SHF  
86 and induces a positive mid-tropospheric geopotential anomaly, the development of a planetary  
87 wave train, a cyclonic anomaly over the Southern Great Plains and the favouring of positive boreal  
88 summer rainfall anomalies (Xue et al. 2016, 2018). Similar to mountainous regions in western

89 North America, the TP is also a high elevated region at a similar latitude to the sub-tropical jet.  
90 It is hypothesised that mechanisms responsible for atmospheric changes that occur across the TP  
91 and south-east Asia, associated with anomalous land surface characteristics, are similar to those  
92 observed in North America.

93 Heat lows are common across sub-tropical arid and semi-arid regions during months of high  
94 insolation. To understand heat lows across the TP, previous studies analysing heat lows in other  
95 sub-tropical regions can be drawn upon. Heat lows have been observed and analysed across  
96 West Africa (Parker et al. 2005; Sultan et al. 2007; Lothon et al. 2008), Angola (Howard and  
97 Washington 2018), the Iberian Peninsula (Hoinka and Castro 2003), and Pakistan/north-west India  
98 (Bollasina and Nigam 2011) amongst other locations. Idealised modelling studies have focused  
99 on understanding heat low dynamics across western Australia (Rácz and Smith 1999; Spengler  
100 et al. 2005) and regions of high elevation (Smith and Spengler 2011). Heat lows are formed when  
101 strong solar surface heating leads to ascent and increased low-level relative vorticity. Even though  
102 low-level atmospheric temperatures maximise during the afternoon alongside a surface pressure  
103 minima at the centre of heat lows, boundary-layer turbulence inhibits and delays a low-level  
104 wind response. As a result, low-level convergence and relative vorticity do not maximise until  
105 nighttime, once insolation is removed and boundary-layer turbulence is much weaker (Rácz  
106 and Smith 1999; Parker et al. 2005; Smith and Spengler 2011; Howard and Washington 2018).  
107 Above the heat low, an anticyclone develops associated with upper-level divergence. Upper-level  
108 anticyclone characteristics have smaller diurnal variations compared to the low-level cyclone due  
109 to a reduced influence of diurnally-varying boundary-layer turbulence at altitude (Rácz and Smith  
110 1999; Howard and Washington 2018). Idealised modelling experiments have also been performed  
111 to investigate the sensitivity of heat lows to orography (Smith and Spengler 2011). When applying  
112 identical surface heating to elevated and low regions, greater decreases in low-level air density are



113 simulated over elevated regions associated with a shallower atmosphere. The horizontal gradient  
114 in atmospheric density enhances low-level convergence and promotes an intensified heat low  
115 across elevated slopes. There are currently a small number of studies analysing the impact of  
116 intraseasonal soil moisture variations on the development of heat lows across semi-arid regions  
117 (Taylor 2008; Lavender et al. 2010). In this study we highlight the influence of intraseasonal soil  
118 moisture variability on heat low development across the TP using observations and reanalysis.

119 Modelling experiments highlight a sensitivity of local atmospheric conditions to TP surface  
120 warming (Wang et al. 2008; Liu et al. 2012; Wan et al. 2017; Ge et al. 2019). Increased TP surface  
121 warming promotes a heat low circulation associated with an anomalous low-level cyclone and an  
122 anomalous upper-level anticyclone (Wang et al. 2008; Wan et al. 2017; Ge et al. 2019). Alongside  
123 a local atmospheric response to TP surface warming, remote atmospheric conditions are also  
124 impacted (Wang et al. 2008; Wan et al. 2017). Wan et al. (2017) investigated the impact of initial  
125 soil moisture conditions across the TP in the Weather Research and Forecasting (WRF) model on  
126 local and remote atmospheric conditions. Their study was motivated by ten extreme precipitation  
127 events in southeast China, not associated with tropical cyclones, being preceded by anomalous  
128 positive TP near-surface air temperatures of approximately 1 to 2°C five days before. Three  
129 experiments were performed comparing a realistic soil moisture initialisation with idealised wet  
130 and dry soil conditions representing the two extremes in surface hydrology. Dry soil conditions  
131 increase surface SHF, boundary-layer height, and near-surface air temperatures across the TP.  
132 Low-level atmospheric heating induces an anomalous low-level cyclone, associated with positive  
133 temperature anomalies, and an upper-level anticyclone, associated with negative temperature  
134 anomalies. The upper-level anticyclone interacts with the subtropical Eurasian jet and induces  
135 an eastward-propagating Rossby wave, similar to behaviour observed across elevated regions in  
136 North America (Xue et al. 2016, 2018). The subtropical Eurasian jet also promotes the eastward

137 propagation of upper-level negative temperature anomalies. The combination of an upper-level  
138 Rossby wave and upper-level negative temperature anomalies induces a low-level cyclone across  
139 southeast China and extends the subtropical west Pacific high westward over central China. These  
140 two changes restrict the northward propagation of cyclonic circulations that develop in the South  
141 China sea and increase precipitation across southeast China. Changes in precipitation across  
142 China several days after surface drying on the TP highlight that land-atmosphere feedbacks across  
143 the TP can influence precipitation in East Asia.

144 In this study we will show the influence of intraseasonal soil moisture fluctuations across the  
145 TP, predominately controlled by precipitation variations, on the local surface energy balance.  
146 Following this, we will build on simulations analysed in Wan et al. (2017) to investigate the impact  
147 of surface flux variations, induced by soil moisture fluctuations, on heat low development across  
148 the TP and atmospheric conditions across East Asia. Through analysing this series of processes,  
149 we are investigating the full feedback cycle between the atmosphere drying and warming the  
150 surface and the land surface heating the atmosphere and modulating the circulation. Section 2  
151 provides an overview of weather station datasets, satellite products and ERA5 (European Centre  
152 for Medium-Range Weather Forecasts Reanalysis version 5; Copernicus Climate Change Service  
153 (C3S) 2017; Hersbach et al. 2020) reanalysis that are utilised in this study. The results are  
154 presented in section 3 and are split into three components. Section 3a discusses the sensitivity  
155 of surface fluxes to intraseasonal precipitation and soil moisture variability across the TP, whilst  
156 sections 3b and 3c discuss the sensitivity of local and remote, respectively, atmospheric conditions  
157 to TP surface warming. Finally sections 4 and 5 provide a discussion and conclusions.

158

## 2. Methodology

In this study we use a combination of in situ weather station measurements, satellite products, and an atmospheric reanalysis to investigate the impact of soil moisture-atmosphere feedbacks across the TP. A network of 49 stations (cyan squares in Fig. 1a) above 3000m from the China Meteorological Administration (CMA) taking six-hourly (00, 06, 12 and 18 UTC) measurements between 2000 and 2015 of surface temperature ( $T_s$ ), near-surface air temperature ( $T_a$ ), and 10m wind speed ( $v_{10}$ ), alongside daily precipitation accumulations at 12 UTC, are used to analyse surface conditions across the TP. CMA in situ measurements were only available between 2000 and 2015. To increase the number of years of precipitation data across the TP, we use daily precipitation accumulations extracted from APHRODITE (Asian Precipitation - Highly-Resolved Observational Data Integration Towards Evaluation; Yatagai et al. 2012) at  $0.25^\circ$  resolution from 1979 to 2015. APHRODITE is a gridded, continental-scale precipitation and near-surface air temperature product that utilises a dense network of weather stations (Yasutomi et al. 2011; Yatagai et al. 2012). Substantial interpolation is required across the TP due to the small number of weather stations. Values at each  $0.25^\circ$  grid point in APHRODITE are calculated by combining surrounding weather station measurements with locations approximated onto a  $0.05^\circ$  grid (Yatagai et al. 2012). In the case where zero rainfall measurements are taken across the  $0.05^\circ$  grid associated with a  $0.25^\circ$  grid point, interpolation is required from surrounding  $0.25^\circ$  grid values. To minimise the influence of interpolation,  $0.25^\circ$  grid points in APHRODITE are only analysed if they contain measurements for at least one of the  $0.05^\circ$  grid points for a minimum of 95% of boreal summer days between 1979 and 2015. Even though APHRODITE comprises measurements from 26 different countries resulting in different times of day at which readings are taken (Yatagai et al. 2012), no spatial variations in the timing of measurements is recorded. As all measurements in

China are provided by CMA (Yatagai et al. 2012), the same organisation who provided the weather station data, we assume APHRODITE daily precipitation accumulations are computed at 12 UTC. We also use near-surface daily-mean air temperatures from APHRODITE to explore surface conditions during dry spells across the TP.

Several satellite products are used to understand the land surface response to intraseasonal precipitation variability across the TP. Precipitation data retrieved between 2000 and 2015 by the Tropical Rainfall Measuring Mission 3B42 version 7 (TRMM 3B42V7; Huffman et al. 2007) is utilised in this study. TRMM 3B42V7 precipitation data is computed by a combination of passive microwave data from low Earth-orbiting satellites, infrared data collected by the international constellation of geosynchronous earth orbit satellites, and monthly rain gauge data from the Global Precipitation Climatology Project (GPCP; Adler et al. 2003) and National Oceanic and Atmospheric Administration (NOAA) Climate Prediction Center (Huffman et al. 2007). Hourly-mean surface radiative fluxes are extracted from Clouds and the Earth's Radiant Energy System (CERES; Loeb et al. 2003) to understand changes in the surface energy balance across the TP. CERES surface fluxes are derived through combining (Kato et al. 2018): observed filtered top-of-the-atmosphere (TOA) irradiance in the shortwave and longwave (Loeb et al. 2003); cloud properties retrieved by Moderate Resolution Imaging Spectroradiometer (MODIS) and geostationary satellites (Minnis et al. 2011); and temperature, specific humidity, and ozone profiles from the Goddard Earth Observing System version 5.4.1 reanalysis (Rienecker et al. 2008). Finally, soil moisture anomalies across the TP are computed using satellite retrievals from the European Space Agency Climate Change Initiative (ESA CCI) combined soil moisture product v04.4 (Dorigo et al. 2017; Gruber et al. 2017, 2019). ESA CCI combined soil moisture product v04.4 combines four active and seven passive microwave-based instruments alongside a global land data assimilation system (GLDAS; Rodell et al. 2004) to obtain a consistent climatology throughout the entire time

206 series (Gruber et al. 2019).

207 CMA weather station data is used to approximate outgoing longwave radiation ( $LW_{up}$ ) and sur-  
208 face SHF:

$$LW_{up} = \varepsilon \sigma T_s^4 \quad (1)$$

$$SHF = \rho C_p C_{DH} v_{10} (T_s - T_a) \quad (2)$$

209 where  $\varepsilon$  is the surface emissivity (assumed here to be fixed at 0.95);  $\sigma$  is the Stefan-Boltzmann  
210 constant ( $5.67 \times 10^{-8} \text{ W m}^{-2} \text{ K}^{-4}$ ),  $C_p$  is the specific heat capacity of dry air at constant pressure  
211 and equals  $1005 \text{ J kg}^{-1} \text{ K}^{-1}$ ;  $\rho$  is density ( $\text{kg m}^{-3}$ ) and decreases exponentially with height;  
212  $C_{DH}$  is the drag coefficient for heat and assumed at  $4.0 \times 10^{-3}$  for all stations (following Duan  
213 and Wu 2008);  $v_{10}$  is the mean wind measured at 10m above the ground ( $\text{m s}^{-1}$ );  $T_s$  and  $T_a$  are  
214 the skin and near-surface air temperatures (K) respectively. Combining CERES-derived surface  
215 fluxes with computed  $LW_{up}$  (Eqn. 1) and surface SHF (Eqn. 2) from CMA weather station data  
216 is used to partition the surface energy balance (SEB). The following equation is formulated after  
217 partitioning the SEB into land surface forcings and SEB components that depend on land surface  
218 characteristics:

$$SW_{net} + LW_{down} = LW_{up} + SHF + LHF + G \quad (3)$$

219 where  $SW_{net}$  denotes the surface net-downward shortwave radiation ( $\text{W m}^{-2}$ );  $LW_{down}$  denotes the  
220 surface downward longwave radiation ( $\text{W m}^{-2}$ ); LHF denotes the latent heat flux ( $\text{W m}^{-2}$ ); and  $G$   
221 denotes the ground heat flux ( $\text{W m}^{-2}$ ). If we assume that sub-seasonal changes in surface albedo  
222 are minimal, components on the right-hand side of (Eqn. 3) do depend on sub-seasonal changes

in surface characteristics whilst components on the left-hand side do not. Upon subtracting SHF and  $LW_{up}$  from CERES-derived surface radiation, the remainder is assumed to be a combination of LHF and G. In this study we only consider instantaneous surface fluxes at 18 UTC. We approximate instantaneous CERES-derived radiative fluxes by averaging hourly-mean retrievals at 1730 and 1830 UTC.

We use ERA5 reanalysis (Copernicus Climate Change Service (C3S) 2017; Hersbach et al. 2020) to investigate the influence of soil moisture-atmosphere interactions across the TP on local and remote atmospheric conditions. ERA5 data is analysed at a three-hourly  $1^\circ$  resolution on twenty pressure levels (50 to 1000hPa in increments of 50hPa). ERA5, computed using 4D-Var data assimilation and cycle 41r2 of the Integrated Forecasting System (IFS), provides a detailed record of the global atmosphere, land and ocean waves (Hersbach et al. 2018, 2020). At the time of access, ERA5 data was only available from 1979. Finally, due to the large longitudinal range with which Beijing Time (BT) is used across China, it is inappropriate to use BT as a reference for local solar conditions across the TP. In light of this we refer to the local solar time (LST) which is six hours ahead of UTC as the eastern TP is approximately situated at  $90^\circ$  longitude (Fig. 1a).

### 3. Results

#### *a. Surface response to intraseasonal precipitation variability*

##### 1) INTRASEASONAL PRECIPITATION VARIABILITY

We first quantify boreal summer intraseasonal precipitation variability across the TP and east Asia (Fig. 1). To compute the annual-mean power associated with intraseasonal Boreal summer rainfall variability, the daily precipitation anomaly is standardised using the non-zero mean precipitation rate. Intraseasonal rainfall variability, shown in Figure 1a, is the total power

245 associated with modes between 7 and 30 days when performing a discrete Fourier transform on  
 246 the standardised daily precipitation anomaly. In agreement with previous studies (Wang and Duan  
 247 2015), both standardised satellite and weather station data illustrate substantial intraseasonal  
 248 precipitation variability across the TP (Fig. 1a, b). In comparison with intraseasonal precipitation  
 249 variability across the rest of East Asia, the TP stands out along with the Indian monsoon core zone  
 250 (approximately 16 to 22°N and 75 to 85°E; Mandke et al. 2007), associated with active and break  
 251 spells of the Indian summer monsoon (Rajeevan et al. 2010; Singh et al. 2014), and the coast of  
 252 Myanmar (approximately 20°N and 95°E), associated with orographically-driven precipitation  
 253 (Shige et al. 2017). Greater daily precipitation accumulations over the ocean compared to land  
 254 lead to a substantial land-sea contrast in intraseasonal precipitation variability. Note that the  
 255 stronger power at intraseasonal timescales in CMA compared to APHRODITE (Fig. 1b) is due to  
 256 APHRODITE being a gridded dataset whilst CMA is a set of localised weather stations (section  
 257 2).

258 We now exploit the availability of a network of long-term in situ surface temperature measure-  
 259 ments from CMA and satellite soil moisture observations to examine the land surface response  
 260 to intraseasonal precipitation variability across the TP. An initial look at a typical summer season  
 261 (JJA 2013) illustrates that intraseasonal soil moisture fluctuations across the TP are strongly  
 262 controlled by precipitation variations. As well as this, substantial changes in the five-day  
 263 running-mean 12 LST surface temperature anomalies are broadly out of phase with rainfall (Fig.  
 264 1c). During periods of minimal rainfall, i.e. mid-June 2013, surface soil moisture decreases and  
 265 skin temperature anomalies of approximately +10°C are observed at 12 LST. During wet periods,  
 266 i.e. the majority of July 2013, surface soil moisture increases and negative skin temperatures  
 267 anomalies of approximately -5°C are observed at 12 LST. Substantially smaller skin temperature  
 268 anomalies are observed at other times of the day illustrating a diurnally-varying sensitivity of the

land surface to precipitation variability associated with the diurnal cycle of insolation. This time series suggests a strong sensitivity of daytime surface heating across the TP to dry events and qualitatively, similar features are found in every boreal summer of the CMA dataset (not shown).

## 2) STATION-SCALE LAND SURFACE RESPONSE TO DRY EVENTS

To better understand the surface response to precipitation variability across the TP, a dry event composite is computed at each CMA weather station. Daily precipitation accumulations are used to identify “dry events”. Similar to Gallego-Elvira et al. (2016), a dry event is defined when the initial precipitation rate is above  $5 \text{ mm day}^{-1}$  and succeeded by a least two days with less than  $1 \text{ mm day}^{-1}$ . In Gallego-Elvira et al. (2016), a maximum threshold of  $0.5 \text{ mm day}^{-1}$  is used to define a dry day. However, when compositing CMA weather station data this threshold gave a small number of dry events. In CMA approximately 3800 two-day dry events are observed between 2000 and 2015 with the number of dry events decreasing exponentially with dry event length (Fig. 2). We also composite the nearest ESA CCI soil moisture observation to each weather station during a dry event. Note that there are approximately 62% fewer observations of soil moisture than temperature in this composite due to limited availability in the ESA CCI dataset.

Compositing dry events across all weather stations illustrates a strong sensitivity of soil moisture and daytime skin temperatures to prolonged periods of minimal rainfall (Fig. 2a). As the surface dries, peak daytime skin temperatures increase by approximately  $10^{\circ}\text{C}$  in five days. The same diurnal variability is observed in near-surface air temperatures but to a smaller amplitude (only approximately  $2^{\circ}\text{C}$  in five days). As the surface SHF depends on the temperature difference between the ground and near-surface, Fig. 2a indicates that increasing daytime near-surface air temperatures during a prolonged period of minimal rainfall is surface-driven.



292 As expected from the smaller sensitivity of near-surface air temperatures to minimal precipita-  
 293 tion compared to surface temperatures (Fig. 2a), anomalous daytime surface SHF increases with  
 294 dry event length (Fig. 2b). Increasing surface temperatures are also associated with increasing  
 295  $LW_{up}$ . After five days of minimal rainfall, both SHF and  $LW_{up}$  have increased to approximately  
 296  $50 \text{ W m}^{-2}$ . The initial high precipitation accumulation at the start of a dry event is associated  
 297 with cloud cover and daytime surface radiation anomalies of approximately  $-70 \text{ W m}^{-2}$ . Surface  
 298 radiation anomalies then increase to approximately  $70 \text{ W m}^{-2}$  by day 2 and remain relatively  
 299 constant throughout the remainder of the dry event. As the inputted radiation anomaly remains  
 300 relatively constant throughout the dry event composite, increased SHF and  $LW_{up}$  is associated  
 301 with decreased LHF and G in order to maintain surface energy balance. This shows that the evap-  
 302 orative fraction, the fraction of turbulent energy fluxes used for evaporation, decreases as the dry  
 303 spell length increases following high values on days 0 and 1. Even over short dry spells of two  
 304 to three days, reduced soil moisture drives a shift in the partitioning of fluxes from latent to sen-  
 305 sible heat. This is consistent with satellite-based analysis across semi-arid regions of the world  
 306 (Gallego-Elvira et al. 2016). We also considered whether our dry spell flux composite was repre-  
 307 sentative of all sites, or just those in climatologically drier regions. Compositing data from only  
 308 the 10 wettest stations (boreal summer seasonal mean rainfall  $\geq 2.27 \text{ mm day}^{-1}$ ), we still found  
 309 a clear dry spell imprint on evaporative fraction (not shown), albeit of a slightly weaker amplitude  
 310 than the full station composite, as expected.

### 311 3) REGIONAL SURFACE RESPONSE TO DRY EVENTS

312 Individual weather stations highlight a sensitivity of local surface characteristics and SEB  
 313 components to a prolonged period of minimal rainfall. In this subsection we investigate diurnal  
 314 variations in land surface characteristics on a regional scale. We expect these to differ quantita-

315 tively due to the spatial scaling properties of rainfall.

316 Regional dry events are identified when the station-mean daily precipitation accumulation is  
317 below the boreal summer station-mean twentieth percentile for three consecutive days, having  
318 first removed periods with zero rainfall before calculating percentiles. Using this threshold for  
319 rainfall and dry event length reveals a suitable number of dry events across the TP required to  
320 obtain a substantial surface response. Thirty-seven three-day regional dry events are identified  
321 in the CMA dataset. During days of minimal precipitation, the composite-mean, station-mean  
322 daytime CMA near-surface air temperature anomalies increase to approximately  $1.5^{\circ}\text{C}$  (Fig. 3a).  
323 As seen on a localised scale (Fig. 2), skin temperatures are more sensitive to minimal rainfall  
324 than near-surface air temperatures with a peak anomaly just below  $6^{\circ}\text{C}$  (Fig. 3a). Focusing on  
325 SEB components observed at 12 LST highlights that the difference between anomalous skin  
326 and near-surface air temperatures is associated with an increased surface SHF of approximately  
327  $45 \text{ W m}^{-2}$  and a decreased LHF and G total by approximately  $50 \text{ W m}^{-2}$  (Fig. 3b). During  
328 the dry event, anomalous daytime LHF decreases associated with surface drying; surface soil  
329 moisture observations from ESA CCI highlight a 10% reduction between the start and end  
330 of a three-day regional dry event (Fig. 3a). Surface soil moisture values from ERA5 and the  
331 Global Land Data Assimilation System (GLDAS) Noah Land Surface Model (Rodell et al.  
332 2004) also reveal a similar sensitivity of soil moisture to regional dry spells (not shown). The  
333 diurnally-varying sensitivity of near-surface air and skin temperatures (Fig. 3a) is associated with  
334 a diurnally-varying sensitivity of SEB components (not shown). In the following section the  
335 sensitivity of the regional circulation to surface warming and increased surface SHF, associated  
336 with minimal precipitation and surface drying, is investigated.

337 Weather station data from CMA highlights the sensitivity of SEB components to minimal  
338 precipitation. However, due to data only being available from 2000 to 2015 (section 2), only 37

regional dry events are observed. To increase the number of regional dry events a composite using precipitation accumulations since 1979 from APHRODITE is produced. Seventy-two regional dry events are observed in APHRODITE, just under double the number of events observed in CMA. At a local scale the sensitivity of daily-mean near-surface air temperatures to minimal rainfall is similar in APHRODITE and CMA (Fig. 4). After five days of minimal rainfall, near-surface daily-mean air temperature anomalies are approximately 1.3°C in both datasets. After seven days of minimal rainfall, daily-mean air temperature anomalies continue to increase in CMA but plateau in APHRODITE, associated with a smaller number of localised dry events lasting longer than seven days in APHRODITE. Because the CMA and APHRODITE datasets share a similar sensitivity of daily-mean near-surface air temperature anomalies to minimal precipitation, we assume that the sensitivity of surface temperatures and SEB components is similar in regional dry events extracted from both datasets. As APHRODITE contains nearly double the number of three-day regional dry events compared to CMA (Fig. 3), the rest of this study focuses on regional dry events identified in APHRODITE.

#### *b. Influence of TP surface warming on regional atmospheric conditions*

In this section we consider how enhanced daytime surface heating on the TP during three-day regional dry events feeds back onto the atmosphere. However, we first examine the large-scale atmospheric conditions at the start of a regional dry event. At 200 hPa the beginning of a three-day dry event is associated with anomalous north-easterly winds across the western TP, an anomalous cyclone across east TP, and an anomalous anticyclone northwest of TP (Fig. 5a). The anomalous upper-level circulation pattern observed at the start of regional dry events is associated with the Silk Road pattern (SRP) teleconnection (Lu et al. 2002; Enomoto et al. 2003; Hsu and Lin 2007).

362 Forced by diabatic heating across the Eurasian continent (Hsu and Lin 2007), the SRP develops  
363 during boreal summer and is associated with a propagating Rossby wave along the subtropical  
364 Eurasian jet (Lu et al. 2002; Enomoto et al. 2003). The propagation of the SRP onto the TP is  
365 best observed in the vertically-averaged upper-tropospheric meridional wind (Fig. 6a). Significant  
366 meridional wind and geopotential anomalies are observed over Europe five to eight days before  
367 a dry event across the TP. At 500 hPa, approximately just above the east TP surface, anomalous  
368 northerly winds dominate at the beginning of a dry event associated with an anomalous anticy-  
369 clone (Fig. 5b).

370 Temperature anomalies at 500 hPa across the TP during regional dry events increase by approx-  
371 imately 2.5°C (Fig. 6e). As surface warming peaks during daytime hours of regional dry events,  
372 we investigate sub-daily variations in atmospheric conditions to try to identify the surface influ-  
373 ence on local atmospheric conditions. Sub-daily temperature variations at 500 hPa highlight that  
374 low-level warming predominately occurs during daytime hours (red line in Fig. 7a). The depth  
375 of positive temperature tendencies increases as the day progresses associated with a deepening  
376 boundary-layer (Figs. 7a and 8). Sub-daily tendencies in anomalous temperatures across the TP  
377 during regional dry events are similar to those in heat low studies that use idealised experiments  
378 (Rácz and Smith 1999; Smith and Spengler 2011) and observations (Hoinka and Castro 2003;  
379 Parker et al. 2005; Howard and Washington 2018). Sub-daily variations in geopotential height  
380 and surface pressure also resemble heat low characteristics with reductions in surface pressure and  
381 low-level geopotential height occurring after sunset (Fig. 7b, c). As described in Rácz and Smith  
382 (1999), substantial surface warming drives boundary-layer turbulence during the daytime which  
383 restricts a horizontal wind response to the developed pressure gradient. Once insolation is removed  
384 and the surface cools, a stable surface layer develops. This leads to minimal boundary-layer turbu-  
385 lence, allowing the horizontal flow to strengthen. Low-level zonal convergence and vertical ascent

386 develop in the evening across the eastern TP, with the latter extending to 200 hPa (Fig. 8h). The  
387 low-level (500 hPa) flow becomes more geostrophic during the evening and generates positive  
388 low-level relative vorticity (Fig. 9d).

389 Above the heat low an anticyclone develops at approximately 200 hPa associated with negative  
390 temperature tendencies (Fig. 8). Upper-level anticyclone characteristics vary diurnally, with posi-  
391 tive geopotential tendencies reaching their maximum during the afternoon and evening (Fig. 8f, h)  
392 associated with sub-daily variations in mid-tropospheric warming between 250 and 400 hPa (Fig.  
393 8e, g). Diurnal variations in upper-level anticyclonic characteristics are inconsistent with mod-  
394 elling work performed by Rácz and Smith (1999) due to diurnal variations in mid-tropospheric  
395 heating. Different mechanisms are responsible for mid-tropospheric heating during the afternoon  
396 and evening. In the afternoon mid-tropospheric warming is associated with a deepening of the  
397 boundary-layer, whilst mid-tropospheric warming during the evening, is associated with increased  
398 mid-tropospheric shear turbulence due to difference in wind direction between the sub-tropical  
399 westerly jet and easterly component of low-level convergence. Not only does anomalous turbulent  
400 mixing increase mid-tropospheric temperatures, but it also increases mid-tropospheric zonal wind  
401 (Fig. 8g) due to the downward transport of zonal momentum from the sub-tropical westerly jet  
402 (Fig. 10a). Warming between 250 and 400 hPa alongside cooling at 150 hPa increases geopo-  
403 tential height at 200 hPa. As expected, upper-level relative vorticity tendencies are also strongest  
404 during the afternoon and evening (not shown).

405 Regional-scale three-day dry spells across the TP, initially driven by upper-tropospheric geopo-  
406 tential anomalies, lead to surface warming, the formation of a heat low, and positive upper-level  
407 geopotential tendencies. In the following section we investigate the influence of positive geopoten-  
408 tial upper-tropospheric tendencies, associated with the development of a heat low, on the remote  
409 circulation and weather conditions across east Asia.

410 *c. Influence of TP surface warming on remote atmospheric conditions*

411 Regional dry events across the TP favour the development of a heat low (section 3b). It is  
412 challenging to isolate the influence of anomalous atmospheric conditions across the TP on the  
413 remote atmospheric circulation using observations alone due to the influence of other factors,  
414 notably the large-scale circulation. However, Wan et al. (2017) performed modelling sensitivity  
415 experiments to investigate the influence of soil moisture across the TP on atmospheric conditions  
416 during an extreme rainfall event in southeast China. In this section we will compare remote  
417 atmospheric changes observed in our regional dry spell composite with the sensitivity of remote  
418 atmospheric conditions to TP soil moisture in Wan et al. (2017).

419 In Wan et al. (2017) extreme decreases in soil moisture across the TP increase surface SHF and  
420 lead to the development of a heat low. The heat low influences remote atmospheric conditions  
421 through two mechanisms: (1) the development of an upper-level planetary Rossby wave train; and  
422 (2) the eastward propagation of upper-level negative temperature anomalies. During our regional  
423 dry event composite negative upper-level geopotential tendencies are observed east of the TP  
424 alongside positive upper-level geopotential tendencies further east (Figs. 5c and 6b). The diurnal  
425 cycle of geopotential tendencies is approximately 20% greater east of the TP during the afternoon  
426 and evening (Fig. 8), the same time period where geopotential tendencies maximise due to the  
427 development of a heat low. Both of these factors are indicative of a Rossby wave forcing. In  
428 our composite the upper-level Rossby wave forcing associated with the heat low intensifies an  
429 upper-level cyclone east of TP across central China (Figs. 5c, 6b). The intensified upper-level  
430 cyclone also decreases geopotential height at 500 hPa, and by the end of the dry spell, significant  
431 negative geopotential anomalies are observed across central China at 200 and 500 hPa (Figs.  
432 5 and 6). The upper-level Rossby wave forcing observed in our regional dry event composite

433 agrees well with Wan et al. (2017). However, Wan et al. (2017) show an intensified cyclone at  
434 850 hPa over southeast China, meanwhile in our composite, geopotential height anomalies at  
435 850 hPa are minimal at the end of dry events (Fig. 10d). It may also be argued that the SRP is  
436 solely responsible for geopotential tendencies observed. However, as upper-level anomalies in  
437 meridional wind and geopotential height dramatically decrease after day 3 (Fig. 6a, b), we infer  
438 that the SRP is not solely responsible for upper-level geopotential anomalies downstream of the  
439 TP during dry spells.

440 Alongside an immediate atmospheric response to heat lows across the TP due to Rossby wave  
441 forcing, the remote atmosphere is also influenced several days after regional dry events. Negative  
442 upper-level temperature anomalies associated with heat lows (Figs. 7a and 10c) propagate along  
443 the sub-tropical jet (Fig. 10a) reaching southern China three days after minimal precipitation  
444 across the TP (Figs. 6d and 10e). This advected cool upper-level air increases geopotential  
445 height beneath it and favours a westward extension of the western north Pacific sub-tropical  
446 high (Fig. 10f). In Wan et al. (2017) the advection of cool air generates positive geopotential  
447 height anomalies across central China, whilst in our dry event composite low-level geopotential  
448 height anomalies are much smaller and located over central and southern China (Fig. 10f). Even  
449 increasing the length of regional dry events to promote further surface drying across the TP and  
450 leading to surface soil moisture anomalies more similar to Wan et al. (2017), has a minimal effect  
451 on remote geopotential height anomalies (not shown). Advection of negative vorticity from an  
452 anticyclone northwest of TP (Fig. 5b) along the sub-tropical jet (Fig. 10a) leads to a broad region  
453 of positive geopotential anomalies across northern China (Fig. 5e, f).

454 To conclude our analysis we examine the association of dry events across the TP with weather  
455 conditions across East Asia. Dry events across the TP are associated with a dipole in daily-mean  
456 temperature changes (Fig. 11b, d, f, h). Several days after dry events across the TP, daily-mean

457 temperatures increase by  $1.2^{\circ}\text{C}$  across central and eastern China and decrease by  $0.5^{\circ}\text{C}$  in  
 458 southeast China and the Indochinese peninsula. Figure 11h highlights that surface-atmosphere  
 459 interactions across the TP during dry spells significantly increases near-surface temperatures  
 460 across heavily populated and agriculturally intensive regions of East Asia. In Wan et al. (2017)  
 461 reducing soil moisture across the TP increases total and extreme precipitation in southeast China.  
 462 In our study a dipole in mean precipitation changes is observed several days after surface drying  
 463 across the TP (Fig. 11a, c, e, g). Across central and eastern China mean precipitation significantly  
 464 decreases whilst precipitation increases in southeast China and the Indochinese peninsula.  
 465 During days 3 and 4 the dipole in mean precipitation changes is associated with an intensified  
 466 cyclone across central China (Fig. 5c, d), whilst by day 6, the westward extension of the west  
 467 Pacific sub-tropical high (Fig. 10f) restricts northward moisture propagation and increases  
 468 precipitation across southern China. Wan et al. (2017) highlight an increased probability of  
 469 extreme precipitation in southeast China when drying the TP surface. However in our composite,  
 470 the increased likelihood of extreme precipitation in southeast China is insignificant (not shown).  
 471 There are several reasons for the different responses in extreme precipitation. Firstly, Wan et al.  
 472 (2017) only investigate the influence of soil moisture across the TP during a single extreme  
 473 precipitation event where atmospheric conditions may not be typical for when the TP surface  
 474 is dry. Secondly, soil conditions in our dry event composite are substantially less extreme than  
 475 in sensitivity experiments by (Wan et al. 2017). As a result, surface sensible heat fluxes across  
 476 the TP are much greater in Wan et al. (2017) compared to those in our dry event composite  
 477 (Fig. 3b) by approximately  $70 \text{ W m}^2$ . Finally, the influence of tropical cyclones on extreme  
 478 precipitation rates across East Asia have not been considered in this study. Hence, the influence  
 479 of land-atmosphere interactions across the TP on extreme precipitation rates is challenging to  
 480 detect due to the influence of tropical cyclones. Whilst the influence of dry events across the TP



on extreme precipitation rates requires further investigation, significant mean precipitation and temperature changes highlight the importance of land-atmosphere interactions.

#### 4. Discussion

The warming rate of surface temperatures relative to near-surface air temperatures can be used to highlight the land surface response to dry spells (Gallego-Elvira et al. 2016). Combining in situ weather station measurements with satellite-derived datasets, we have highlighted the sensitivity of land surface characteristics across the TP to even short dry spells of two to three days. In situ measurement shown here reveal an average relative warming rate of approximately  $0.38 \text{ K day}^{-1}$  across the eastern TP for dry spells of approximately five days. During periods of minimal rainfall across the TP, surface LHF is limited, due to soil moisture availability, and surface SHF increases. In general, changes in evaporative fraction during dry spells are difficult to capture in climate models (Gallego-Elvira et al. 2019). Given the feedback on the atmosphere by the flux response to surface drying across the TP shown here and previous studies (Wan et al. 2017; Xue et al. 2018), analysis of model depictions of TP dry spells is warranted.

Through investigating the sensitivity of local atmospheric conditions to regional dry events across the TP we diagnose the formation of heat lows. In agreement with idealised modelling studies (Rácz and Smith 1999; Spengler et al. 2005; Smith and Spengler 2011) and observations of heat lows in other sub-tropical regions (Parker et al. 2005; Bollasina and Nigam 2011; Howard and Washington 2018), land-atmosphere interactions play a crucial role in the diurnal cycle of heat low characteristics. Whilst daytime surface heating reaches its maximum during the afternoon, boundary-layer turbulence inhibits a low-level horizontal wind response. Once insolation is removed and a stable surface layer develops, low-level horizontal convergence and relative

504 vorticity maximises. This is the first study to show how dry spells across the TP influence the  
505 diurnal cycle of heat lows. Even though idealised modelling studies conclude a minimal diurnal  
506 cycle of upper-level anticyclonic characteristics (RÁCZ and Smith 1999; Smith and Spengler  
507 2011), we find that mid-tropospheric heating during the afternoon and evening, associated with  
508 increases in boundary-layer depth and mid-tropospheric turbulent mixing, result in sub-daily  
509 variations in anticyclonic characteristics.

510 The influence of land-atmosphere interactions on other circulation systems across the TP re-  
511 mains to be investigated. For example, Tibetan Plateau vortices (TPVs) are mesoscale circulations  
512 distinguished by substantial low-level relative vorticity and responsible for a substantial fraction  
513 of precipitation across the TP (Curio et al. 2019). In this study surface drying increases low-level  
514 relative vorticity thereby motivating future work to investigate the influence of land-atmosphere  
515 interactions in the development and intensity of TPVs. Recent studies have also shown that  
516 soil moisture gradients across the TP favour the initiation of convective systems (Barton et al.  
517 submitted).

518 Soil moisture-atmosphere interactions during dry events across the TP also influence atmo-  
519 spheric and weather conditions across east Asia. Previous observational and modelling studies  
520 have shown how large-scale surface temperature anomalies across the TP promote an atmospheric  
521 stationary wave that extends eastward from the original surface temperature anomaly (Wan et al.  
522 2017; Xue et al. 2018). Our results are consistent with these findings. Future work should  
523 investigate whether these soil moisture-atmosphere feedbacks are observed in weather forecasting  
524 models to improve sub-seasonal forecasting capabilities across East Asia.

525 The sensitivity of remote atmospheric conditions to surface drying across the TP is substantially  
526 different in our dry event composite compared to sensitivity experiments performed by Wan et al.  
527 (2017). The difference in atmospheric response is most likely associated with the magnitude

of soil moisture forcing in these two studies. In Wan et al. (2017) soil moisture is reduced to  
the surface layer's wilting point, effectively fixing evapotranspiration to zero. In our dry event  
composite soil moisture fluctuations are much smaller and the change in latent heat flux is  
approximately  $70 \text{ W m}^{-2}$  smaller compared to latent heat flux changes when drying the TP in  
Wan et al. (2017). We therefore conclude that it is unrealistic to fix evapotranspiration to zero  
across the TP and the difference in soil moisture fluctuations leads to a much greater surface and  
atmospheric response in Wan et al. (2017). For example, the difference in surface SHF between  
a normal and dry TP surface is approximately three times greater in Wan et al. (2017) compared  
to anomalies observed in our dry event composite. Stronger surface SHF anomalies in Wan et al.  
(2017) promote an intensified localised heat low, colder upper-level temperature anomalies, and  
increased low-level geopotential height tendencies across east Asia. The westward extension  
of the western North Pacific sub-tropical high is further north in Wan et al. (2017) compared  
to changes observed in our dry event composite. This may be due to Wan et al. (2017) only  
performing sensitivity experiments for a single persistent heavy precipitation event in south-east  
China. The different atmospheric mean states and fluctuations in land surface characteristics  
between this study and sensitivity experiments analysed in Wan et al. (2017), vary the influence  
of land-atmosphere interactions across the TP on extreme precipitation events across east Asia.  
Surface conditions across East Asia may influence the atmospheric response to dry spells across  
the TP. For example, it may be the case that near-surface warming across north China several days  
after a TP dry spell would be larger during a local drought. However, the small number of dry  
spells in our sample precludes further subsetting. We would recommend a modelling approach to  
understand this dependence. Work in this study and by Wan et al. (2017) highlight the importance  
of land-atmosphere interactions across the TP in determining weather conditions across east Asia.  
Improving the simulation of land-atmosphere interactions across the TP at all time scales may

552 lead to improvements in climate models over a much larger region. Warming across the TP  
553 provides a heat source in the mid-latitudes that intensifies the Indian monsoon (Kutzbach et al.  
554 1993; Molnar et al. 1993; Zhisheng et al. 2001). Improving the sensitivity of surface temperatures  
555 to intraseasonal precipitation variability across the TP may intensify the Indian monsoon and  
556 partly improve the long-standing boreal summer dry bias across the Indian continent (Sperber  
557 et al. 2013; Bush et al. 2015). The influence of intraseasonal fluctuations in land surface char-  
558 acteristics across the TP should also be considered when predicting the atmospheric response to  
559 anthropogenic climate change across east Asia. Not only has anthropogenic climate change been  
560 associated with surface warming across the TP (Wang et al. 2008), but also substantial glacial  
561 loss (Yao et al. 2007, 2012), which may increase the area of semi-arid land and intraseasonal  
562 variability of surface fluxes. An increased influence of the TP land surface on local and remote  
563 atmospheric conditions may change weather conditions across east Asia.

## 565 **5. Conclusions**

566 Using a combination of weather station data and satellite observations we show that soil  
567 moisture and surface fluxes across the TP are sensitive to intraseasonal precipitation variability.  
568 Decreases in soil moisture during dry spells of even two to three days drive increases in surface  
569 temperatures and sensible heat fluxes. Atmospheric reanalysis shows how the anomalous surface  
570 warming feeds back onto the atmosphere and promotes the development of a heat low across the  
571 TP. Consistent with studies from other parts of the world, we illustrate strong diurnal variations in  
572 heat low characteristics. During daytime hours anomalous surface warming increases boundary-  
573 layer temperatures. However, boundary-layer turbulence restricts a low-level wind response until  
574 the surface cools and a stable layer develops. As a result, low-level horizontal convergence and

575 relative vorticity reach their maximum after sunset along with a reduction in surface pressure.  
576 Above the boundary-layer, heat lows promote an anticyclone associated with negative temperature  
577 anomalies. The local atmospheric response to surface warming due to precipitation variability  
578 across the TP highlights the importance of land-atmosphere interactions.

579 The development of heat lows across the TP also influences remote atmospheric conditions. The  
580 development of an upper-level anticyclone during dry spells promotes an upper-level stationary  
581 wave that intensifies a cyclonic circulation across central China. Negative temperature anomalies,  
582 associated with the upper-level anticyclone, propagate along the sub-tropical Eurasian jet towards  
583 south-east China, associated with a westward extension of the western North Pacific subtropical  
584 high. Both the intensification of a cyclonic circulation across central China and the westward  
585 extension of the western North Pacific subtropical high significantly impact weather conditions  
586 in east Asia. Understanding of land-atmosphere interactions across the TP is thus important  
587 for short-term weather forecasting across East Asia. Given the rapidly changing nature of the  
588 hydrological cycle on the TP in response to anthropogenic warming, it may also be relevant for  
589 climate projections across the region. Future work should therefore investigate the simulation of  
590 these soil moisture-atmosphere interactions in both weather and climate models.

591

592 *Acknowledgments.* This work and its contributors (JT, CT, AD, AT) were supported by the  
593 UK-China Research & Innovation Partnership Fund through the Met Office Climate Science for  
594 Service Partnership (CSSP) China as part of the Newton Fund.

595 The authors would like to express their gratitude to those at the Chinese Meteorological  
596 Administration for providing weather station data. APHRODITE precipitation and temperature  
597 data was accessed at <http://www.chikyu.ac.jp/>. TRMM 3B42V7 and CERES satellite products

598 were obtained from the NASA/Goddard Earth Sciences Data and Information Services Center  
599 (GES-DISC). ESA CCI soil moisture satellite data and ERA5 reanalysis data was accessed at  
600 <https://www.esa-soilmoisture-cci.org/> and <https://cds.climate.copernicus.eu/cdsapp/home> respec-  
601 tively. We also thank three anonymous reviewers for their comments.

602

## 603 **References**

- 604 Adler, R. F., and Coauthors, 2003: The version-2 global precipitation climatology project (GPCP)  
605 monthly precipitation analysis (1979–present). *Journal of Hydrometeorology*, **4** (6), 1147–1167.
- 606 Barton, E., C. Taylor, C. Klein, P. Harris, and X. Meng, submitted: Observed soil moisture impact  
607 on strong convection over mountainous Tibetan Plateau. *Journal of Hydrometeorology*.
- 608 Berg, A., B. R. Lintner, K. L. Findell, S. Malyshev, P. C. Loikith, and P. Gentine, 2014: Impact of  
609 soil moisture–atmosphere interactions on surface temperature distribution. *Journal of Climate*,  
610 **27** (21), 7976–7993.
- 611 Bollasina, M., and S. Nigam, 2011: The summertime heat low over Pakistan/northwestern India:  
612 evolution and origin. *Climate Dynamics*, **37** (5-6), 957–970.
- 613 Bush, S. J., A. G. Turner, S. J. Woolnough, G. M. Martin, and N. P. Klingaman, 2015: The effect  
614 of increased convective entrainment on Asian monsoon biases in the MetUM general circulation  
615 model. *Quarterly Journal of the Royal Meteorological Society*, **141** (686), 311–326.
- 616 Carleton, A. M., D. A. Carpenter, and P. J. Weser, 1990: Mechanisms of interannual variability of  
617 the southwest United States summer rainfall maximum. *Journal of Climate*, **3** (9), 999–1015.

Chiriaco, M., S. Bastin, P. Yiou, M. Haeffelin, J.-C. Dupont, and M. Stéfanon, 2014: European heatwave in July 2006: Observations and modeling showing how local processes amplify conducive large-scale conditions. *Geophysical Research Letters*, **41** (15), 5644–5652.

Copernicus Climate Change Service (C3S), 2017: ERA5: Fifth generation of ECMWF atmospheric reanalyses of the global climate. *Copernicus Climate Change Service Climate Data Store (CDS)*, URL <https://cds.climate.copernicus.eu/cdsapp#!/home>.

Cui, J., L. Tian, Z. Wei, C. Huntingford, P. Wang, Z. Cai, N. Ma, and L. Wang, 2020: Quantifying the controls on evapotranspiration partitioning in the highest alpine meadow ecosystem. *Water Resources Research*, **56** (4), e2019WR024815.

Curio, J., R. Schiemann, K. I. Hodges, and A. G. Turner, 2019: Climatology of Tibetan Plateau vortices in reanalysis data and a high-resolution global climate model. *Journal of Climate*, **32** (6), 1933–1950.

Diallo, I., Y. Xue, Q. Li, F. De Sales, and W. Li, 2019: Dynamical downscaling the impact of spring Western US land surface temperature on the 2015 flood extremes at the Southern Great Plains: effect of domain choice, dynamic cores and land surface parameterization. *Climate Dynamics*, **53** (1-2), 1039–1061.

Dorigo, W., and Coauthors, 2017: ESA CCI Soil Moisture for improved earth system understanding: State-of-the art and future directions. *Remote Sensing of Environment*, **203**, 185–215.

Duan, A., and G. Wu, 2005: Role of the Tibetan Plateau thermal forcing in the summer climate patterns over subtropical Asia. *Climate Dynamics*, **24** (7-8), 793–807.

Duan, A., and G. Wu, 2008: Weakening trend in the atmospheric heat source over the Tibetan Plateau during recent decades. Part I: Observations. *Journal of Climate*, **21** (13), 3149–3164.

640 Enomoto, T., B. J. Hoskins, and Y. Matsuda, 2003: The formation mechanism of the Bonin high  
 641 in August. *Quarterly Journal of the Royal Meteorological Society: A journal of the atmospheric*  
 642 *sciences, applied meteorology and physical oceanography*, **129 (587)**, 157–178.

643 Gallego-Elvira, B., C. M. Taylor, P. P. Harris, and D. Ghent, 2019: Evaluation of regional-scale  
 644 soil moisture-surface flux dynamics in earth system models based on satellite observations of  
 645 land surface temperature. *Geophysical Research Letters*, **46 (10)**, 5480–5488.

646 Gallego-Elvira, B., C. M. Taylor, P. P. Harris, D. Ghent, K. L. Veal, and S. S. Folwell, 2016: Global  
 647 observational diagnosis of soil moisture control on the land surface energy balance. *Geophysical*  
 648 *Research Letters*, **43 (6)**, 2623–2631.

649 Ge, J., Q. You, and Y. Zhang, 2019: Effect of Tibetan Plateau heating on summer extreme precip-  
 650 itation in eastern China. *Atmospheric Research*, **218**, 364–371.

651 Gruber, A., W. A. Dorigo, W. Crow, and W. Wagner, 2017: Triple collocation-based merging of  
 652 satellite soil moisture retrievals. *IEEE Transactions on Geoscience and Remote Sensing*, **55 (12)**,  
 653 6780–6792.

654 Gruber, A., T. Scanlon, R. van der Schalie, W. Wagner, and W. Dorigo, 2019: Evolution of the  
 655 ESA CCI Soil Moisture climate data records and their underlying merging methodology. *Earth*  
 656 *System Science Data*, 1–37.

657 Gutzler, D. S., 2000: Covariability of spring snowpack and summer rainfall across the southwest  
 658 United States. *Journal of Climate*, **13 (22)**, 4018–4027.

659 Hersbach, H., and Coauthors, 2018: Operational global reanalysis: progress, future directions and  
 660 synergies with NWP. **(27)**, doi:10.21957/tkic6g3wm, URL <https://www.ecmwf.int/node/18765>.



661 Hersbach, H., and Coauthors, 2020: The ERA5 global reanalysis. *Quarterly Journal of the Royal*  
662 *Meteorological Society*, **146** (730), 1999–2049.

663 Hoinka, K. P., and M. D. Castro, 2003: The Iberian peninsula thermal low. *Quarterly Journal of*  
664 *the Royal Meteorological Society*, **129** (590), 1491–1511.

665 Howard, E., and R. Washington, 2018: Characterizing the synoptic expression of the Angola low.  
666 *Journal of Climate*, **31** (17), 7147–7165.

667 Hsu, H.-H., and S.-M. Lin, 2007: Asymmetry of the tripole rainfall pattern during the East Asian  
668 summer. *Journal of Climate*, **20** (17), 4443–4458.

669 Hu, Q., and S. Feng, 2004: A role of the soil enthalpy in land memory. *Journal of Climate*, **17** (18),  
670 3633–3643.

671 Huffman, G. J., and Coauthors, 2007: The TRMM multisatellite precipitation analysis (TMPA):  
672 Quasi-global, multiyear, combined-sensor precipitation estimates at fine scales. *Journal of Hy-*  
673 *drometeorology*, **8** (1), 38–55.

674 Jiang, D., Z. Ding, H. Drange, and Y. Gao, 2008: Sensitivity of East Asian climate to the progres-  
675 sive uplift and expansion of the Tibetan Plateau under the mid-Pliocene boundary conditions.  
676 *Advances in Atmospheric Sciences*, **25** (5), 709–722.

677 Kato, S., and Coauthors, 2018: Surface irradiances of edition 4.0 clouds and the earths radiant  
678 energy system (CERES) energy balanced and filled (EBAF) data product. *Journal of Climate*,  
679 **31** (11), 4501–4527.

680 Koster, R., S. Schubert, and M. Suarez, 2009: Analyzing the concurrence of meteorological  
681 droughts and warm periods, with implications for the determination of evaporative regime. *Jour-*  
682 *nal of Climate*, **22** (12), 3331–3341.

683 Kutzbach, J., W. Prell, and W. F. Ruddiman, 1993: Sensitivity of Eurasian climate to surface uplift  
684 of the Tibetan Plateau. *The Journal of Geology*, **101** (2), 177–190.

685 Lavender, S. L., C. M. Taylor, and A. J. Matthews, 2010: Coupled land–atmosphere intraseasonal  
686 variability of the West African monsoon in a GCM. *Journal of climate*, **23** (21), 5557–5571.

687 Li, C., and M. Yanai, 1996: The onset and interannual variability of the Asian summer monsoon  
688 in relation to land–sea thermal contrast. *Journal of Climate*, **9** (2), 358–375.

689 Liu, Y., G. Wu, J. Hong, B. Dong, A. Duan, Q. Bao, and L. Zhou, 2012: Revisiting Asian monsoon  
690 formation and change associated with Tibetan Plateau forcing: II. Change. *Climate Dynamics*,  
691 **39** (5), 1183–1195.

692 Lo, F., and M. P. Clark, 2002: Relationships between spring snow mass and summer precipitation  
693 in the southwestern United States associated with the North American monsoon system. *Journal*  
694 *of Climate*, **15** (11), 1378–1385.

695 Loeb, N. G., N. Manalo-Smith, S. Kato, W. F. Miller, S. K. Gupta, P. Minnis, and B. A. Wielicki,  
696 2003: Angular distribution models for top-of-atmosphere radiative flux estimation from the  
697 Clouds and the Earths Radiant Energy System instrument on the Tropical Rainfall Measuring  
698 Mission satellite. Part I: Methodology. *Journal of Applied Meteorology*, **42** (2), 240–265.

699 Loikith, P. C., and A. J. Broccoli, 2012: Characteristics of observed atmospheric circulation pat-  
700 terns associated with temperature extremes over North America. *Journal of Climate*, **25** (20),  
701 7266–7281.

702 Lothon, M., F. Saïd, F. Lohou, and B. Campistron, 2008: Observation of the diurnal cycle in the  
703 low troposphere of West Africa. *Monthly Weather Review*, **136** (9), 3477–3500.

704 Lu, R.-Y., J.-H. Oh, and B.-J. Kim, 2002: A teleconnection pattern in upper-level meridional wind  
705 over the North African and Eurasian continent in summer. *Tellus A: Dynamic Meteorology and*  
706 *Oceanography*, **54** (1), 44–55.

707 Mandke, S. K., A. Sahai, M. Shinde, S. Joseph, and R. Chattopadhyay, 2007: Simulated changes  
708 in active/break spells during the Indian summer monsoon due to enhanced CO<sub>2</sub> concentrations:  
709 assessment from selected coupled atmosphere–ocean global climate models. *International Jour-*  
710 *nal of Climatology: A Journal of the Royal Meteorological Society*, **27** (7), 837–859.

711 Minnis, P., and Coauthors, 2011: CERES edition-2 cloud property retrievals using TRMM VIRS  
712 and Terra and Aqua MODIS dataPart II: Examples of average results and comparisons with  
713 other data. *IEEE transactions on geoscience and remote sensing*, **49** (11), 4401–4430.

714 Miralles, D., M. Van Den Berg, A. Teuling, and R. De Jeu, 2012: Soil moisture-temperature  
715 coupling: A multiscale observational analysis. *Geophysical Research Letters*, **39** (21).

716 Molnar, P., P. England, and J. Martinod, 1993: Mantle dynamics, uplift of the Tibetan Plateau, and  
717 the Indian monsoon. *Reviews of Geophysics*, **31** (4), 357–396.

718 Notaro, M., and A. Zarrin, 2011: Sensitivity of the North American monsoon to antecedent Rocky  
719 Mountain snowpack. *Geophysical Research Letters*, **38** (17).

720 Parker, D., and Coauthors, 2005: The diurnal cycle of the West African monsoon circulation.  
721 *Quarterly Journal of the Royal Meteorological Society*, **131** (611), 2839–2860.

722 Quesada, B., R. Vautard, P. Yiou, M. Hirschi, and S. I. Seneviratne, 2012: Asymmetric European  
723 summer heat predictability from wet and dry southern winters and springs. *Nature Climate*  
724 *Change*, **2** (10), 736–741.

725 Rácz, Z., and R. K. Smith, 1999: The dynamics of heat lows. *Quarterly Journal of the Royal*  
726 *Meteorological Society*, **125 (553)**, 225–252.

727 Rajeevan, M., S. Gadgil, and J. Bhate, 2010: Active and break spells of the Indian summer mon-  
728 soon. *Journal of Earth System Science*, **119 (3)**, 229–247.

729 Rienecker, M. M., and Coauthors, 2008: The GEOS-5 Data Assimilation System: Documentation  
730 of Versions 5.0. 1, 5.1. 0, and 5.2. 0.

731 Rodell, M., and Coauthors, 2004: The global land data assimilation system. *Bulletin of the Amer-*  
732 *ican Meteorological Society*, **85 (3)**, 381–394.

733 Schumacher, D. L., J. Keune, C. C. Van Heerwaarden, J. V.-G. de Arellano, A. J. Teuling, and  
734 D. G. Miralles, 2019: Amplification of mega-heatwaves through heat torrents fuelled by upwind  
735 drought. *Nature Geoscience*, **12 (9)**, 712–717.

736 Schwingshackl, C., M. Hirschi, and S. I. Seneviratne, 2017: Quantifying spatiotemporal variations  
737 of soil moisture control on surface energy balance and near-surface air temperature. *Journal of*  
738 *Climate*, **30 (18)**, 7105–7124.

739 Shige, S., Y. Nakano, and M. K. Yamamoto, 2017: Role of orography, diurnal cycle, and intrasea-  
740 sonal oscillation in summer monsoon rainfall over the Western Ghats and Myanmar Coast.  
741 *Journal of Climate*, **30 (23)**, 9365–9381.

742 Singh, D., M. Tsiang, B. Rajaratnam, and N. S. Diffenbaugh, 2014: Observed changes in extreme  
743 wet and dry spells during the South Asian summer monsoon season. *Nature Climate Change*,  
744 **4 (6)**, 456.

745 Smith, R. K., and T. Spengler, 2011: The dynamics of heat lows over elevated terrain. *Quarterly*  
746 *Journal of the Royal Meteorological Society*, **137 (654)**, 250–263.

- 747 Spengler, T., M. J. Reeder, and R. K. Smith, 2005: The dynamics of heat lows in simple back-  
748 ground flows. *Quarterly Journal of the Royal Meteorological Society*, **131 (612)**, 3147–3165.
- 749 Sperber, K., H. Annamalai, I.-S. Kang, A. Kitoh, A. Moise, A. Turner, B. Wang, and T. Zhou,  
750 2013: The Asian summer monsoon: an intercomparison of CMIP5 vs. CMIP3 simulations of  
751 the late 20th century. *Climate Dynamics*, **41 (9-10)**, 2711–2744.
- 752 Sultan, B., S. Janicot, and P. Drobinski, 2007: Characterization of the diurnal cycle of the West  
753 African monsoon around the monsoon onset. *Journal of Climate*, **20 (15)**, 4014–4032.
- 754 Taylor, C. M., 2008: Intraseasonal land–atmosphere coupling in the west african monsoon. *Journal*  
755 *of Climate*, **21 (24)**, 6636–6648.
- 756 Wan, B., Z. Gao, F. Chen, and C. Lu, 2017: Impact of Tibetan Plateau surface heating on persistent  
757 extreme precipitation events in southeastern China. *Monthly Weather Review*, **145 (9)**, 3485–  
758 3505.
- 759 Wang, B., Q. Bao, B. Hoskins, G. Wu, and Y. Liu, 2008: Tibetan Plateau warming and precipita-  
760 tion changes in East Asia. *Geophysical Research Letters*, **35 (14)**.
- 761 Wang, M., and A. Duan, 2015: Quasi-biweekly oscillation over the Tibetan Plateau and its link  
762 with the Asian summer monsoon. *Journal of Climate*, **28 (12)**, 4921–4940.
- 763 Wang, Z., A. Duan, and G. Wu, 2014: Time-lagged impact of spring sensible heat over the Tibetan  
764 Plateau on the summer rainfall anomaly in East China: case studies using the WRF model.  
765 *Climate Dynamics*, **42 (11-12)**, 2885–2898.
- 766 Weisheimer, A., F. J. Doblas-Reyes, T. Jung, and T. Palmer, 2011: On the predictability of the  
767 extreme summer 2003 over Europe. *Geophysical Research Letters*, **38 (5)**.

768 Xue, Y., R. Vasic, Z. Janjic, Y. Liu, and P. C. Chu, 2012: The impact of spring subsurface soil  
769 temperature anomaly in the western US on North American summer precipitation: A case study  
770 using regional climate model downscaling. *Journal of Geophysical Research: Atmospheres*,  
771 **117 (D11)**.

772 Xue, Y., and Coauthors, 2016: Spring land temperature anomalies in northwestern US and the  
773 summer drought over Southern Plains and adjacent areas. *Environmental Research Letters*,  
774 **11 (4)**, 044 018.

775 Xue, Y., and Coauthors, 2018: Spring land surface and subsurface temperature anomalies and  
776 subsequent downstream late spring-summer droughts/floods in North America and East Asia.  
777 *Journal of Geophysical Research: Atmospheres*, **123 (10)**, 5001–5019.

778 Yao, T., J. Pu, A. Lu, Y. Wang, and W. Yu, 2007: Recent glacial retreat and its impact on hydro-  
779 logical processes on the Tibetan Plateau, China, and surrounding regions. *Arctic, Antarctic, and*  
780 *Alpine Research*, **39 (4)**, 642–650.

781 Yao, T., and Coauthors, 2012: Different glacier status with atmospheric circulations in Tibetan  
782 Plateau and surroundings. *Nature Climate Change*, **2 (9)**, 663–667.

783 Yasutomi, N., A. Hamada, and A. Yatagai, 2011: Development of a long-term daily gridded tem-  
784 perature dataset and its application to rain/snow discrimination of daily precipitation. *Global*  
785 *Environmental Research*, **15 (2)**, 165–172.

786 Yatagai, A., K. Kamiguchi, O. Arakawa, A. Hamada, N. Yasutomi, and A. Kitoh, 2012:  
787 APHRODITE: Constructing a long-term daily gridded precipitation dataset for Asia based on a  
788 dense network of rain gauges. *Bulletin of the American Meteorological Society*, **93 (9)**, 1401–  
789 1415.

790 Zampieri, M., F. DAndrea, R. Vautard, P. Ciais, N. de Noblet-Ducoudré, and P. Yiou, 2009: Hot  
791 European summers and the role of soil moisture in the propagation of Mediterranean drought.  
792 *Journal of Climate*, **22** (18), 4747–4758.

793 Zhisheng, A., J. E. Kutzbach, W. L. Prell, and S. C. Porter, 2001: Evolution of Asian monsoons and  
794 phased uplift of the Himalaya–Tibetan plateau since Late Miocene times. *Nature*, **411** (6833),  
795 62–66.

## LIST OF FIGURES

- Fig. 1.** (a) Annual-mean power associated with 7 to 30 day variability of standardised JJA TRMM precipitation (filled, dimensionless). Cyan squares illustrate the location of weather stations in CMA whilst blue circles denote grid points in APHRODITE with measurements for a minimum of 95% boreal summer days between 1979 and 2015. TP is denoted by a black 3000 m contour. (b) Station-mean, annual-mean power in CMA (cyan) and APHRODITE (blue) JJA daily precipitation accumulations ( $[\text{mm day}^{-1}]^2$ ). Vertical dashed grey lines denote 7 and 30 days. For both (a) and (b) only data between 2000 and 2015 is shown. (c) 5-day running-mean ESA CCI surface soil moisture observations ( $\text{m}^3 \text{m}^{-3}$ ) and CMA station-mean skin temperature anomalies ( $^{\circ}\text{C}$ ) at 00 (grey), 06 (purple), 12 (orange), and 18 (green) LST during JJA 2013. Cyan bars and blue dots denote CMA and APHRODITE station-mean daily precipitation accumulations ( $\text{mm day}^{-1}$ ) respectively. . . . 41
- Fig. 2.** Mean surface characteristics across all local dry events in boreal summer recorded by the 49 CMA weather stations. (a) Six-hourly anomalous skin (cyan) and near-surface air temperatures ( $^{\circ}\text{C}$ ) along with composite-mean ESA CCI surface soil moisture observations (brown hexagons,  $\text{m}^3 \text{m}^{-3}$ ). (b) 12 LST SEB components including surface upward long-wave radiation ([Eqn. 1], orange), approximated surface SHF ([Eqn. 2], purple), CERES-derived sum of net-downward shortwave and longwave downward radiation (black), and LHF and G (red,  $\text{W m}^{-2}$ ). Box-and-whisker plots denote daily precipitation accumulations ( $\text{mm day}^{-1}$ ) during a dry event and the preceding six days. The orange line denotes the median; the top and bottom of the box denotes the upper and lower quartiles respectively; and the blue whiskers denote the 10th and 90th percentiles. Grey bars denote the number of events recorded for each dry event length. . . . 42
- Fig. 3.** Anomalous station-mean surface characteristics preceding, during, and after a three-day regional dry event in the CMA dataset. A three-day regional dry event is defined when the station-mean precipitation accumulation is smaller than the twentieth percentile of JJA daily station-mean precipitation, denoted by the blue dashed horizontal line, for three days. (a) Anomalous station-mean near-surface air (red) and skin (cyan,  $^{\circ}\text{C}$ ) temperatures along with composite-mean ESA CCI surface soil moisture observations (brown hexagons,  $\text{m}^3 \text{m}^{-3}$ ). (b) Surface upward longwave radiation ([Eqn. 1], orange), approximated surface SHF ([Eqn. 2], purple), CERES-derived sum of net-downward shortwave and longwave downward radiation (black), and LHF and G (red,  $\text{W m}^{-2}$ ). Box-and-whisker plots show station-mean daily precipitation accumulations ( $\text{mm day}^{-1}$ ). The orange line denotes the median; the top and bottom of the box denotes the upper and lower quartiles; and the blue whiskers denote the 10th and 90th percentiles. Filled blue circles denote outliers in precipitation rates. . . . 43
- Fig. 4.** Anomalous daily-mean near-surface air temperatures ( $^{\circ}\text{C}$ , red line) during localised dry events in (a) CMA and (b) APHRODITE. Box-and-whisker plots denote daily precipitation accumulations ( $\text{mm day}^{-1}$ ) during a dry event and the preceding six days. The orange line denotes the median; the top and bottom of the box denotes the upper and lower quartiles respectively; and the blue whiskers denote the 10th and 90th percentiles. Grey bars denote the number of events recorded for each dry event length. . . . 44
- Fig. 5.** Composite-mean anomalies relative to the monthly-mean in geopotential height (m, filled contours) and horizontal wind ( $\text{m s}^{-1}$ , arrows) during days (a, d) 0.0, (b, e) 3.0, and (c, f) 6.0 of the three-day regional dry-spell composite at (a-c) 200 and (d-f) 500 hPa. For each pressure level, different colorbar limits and wind arrow sizes are used. The TP is denoted by a grey 3000m contour in each panel. Vertical blue lines at 75 and 105° longitude highlight TP's western and eastern boundaries. Orange horizontal lines at 30 and 40° latitude denotes the meridional range averaged for Hovmöllers (Fig. 6) and vertical composites (Fig. 8).



844	Only data significant at the 95% confidence level is shown with wind vectors displayed if	
845	significant in either a zonal or meridional direction. . . . .	45
846	<b>Fig. 6.</b> Hovmöllers of ERA5 composite-mean, meridional-mean (30 to 40° latitude) anomalies in	
847	(a) vertically-averaged meridional wind ( $\text{m s}^{-1}$ ) between 200 and 450 hPa, (b, c) geopotential	
848	height (m) at (b) 200 and (c) 500 hPa, and (d, e) temperature ( $^{\circ}\text{C}$ ) at (d) 200 and (e)	
849	500 hPa in the three-day regional dry-event composite. Vertical black dashed lines at 75 and	
850	105° longitude highlight TP's western and eastern boundaries whilst horizontal dashed lines	
851	denote days 0.0 and 3.0 of the regional dry event composite. Stippling denotes anomalies	
852	significant at the 95% confidence level. . . . .	46
853	<b>Fig. 7.</b> Composite-mean, regional-mean (30 to 40° latitude, 90 to 100° longitude) anomalous (a)	
854	temperature ( $^{\circ}\text{C}$ ), (b) geopotential height (m), (c) surface pressure (hPa), and (d) relative	
855	vorticity ( $\text{s}^{-1}$ ) during the three-day regional dry event composite. For a, b, and d, anomalous	
856	values are shown at 500 (red), 400 (orange), 300 (cyan), and 200 (blue) hPa. Box-and-	
857	whisker plots in all panels show station-mean daily precipitation accumulations ( $\text{mm day}^{-1}$ ).	
858	Upper and lower quartiles are denoted by the top and bottom of boxes; box whiskers denote	
859	the 10th and 90th percentiles; and the mean is denoted by an orange line. Background	
860	colours in each panel highlight daytime (yellow, 06 to 18 LST) and nighttime (purple, 18 to	
861	06 LST) hours. . . . .	47
862	<b>Fig. 8.</b> Changes in composite-mean, daily-mean, meridional-mean (30 to 40° latitude) (a, c, e, g)	
863	temperature (filled, $^{\circ}\text{C}$ ), zonal wind (lined, $\text{m s}^{-1}$ ), (b, d, f, i) geopotential height (filled, m),	
864	and vertical wind (lined, $\text{hPa s}^{-1}$ ) between (a, b) 00 to 06, (c, d) 06 to 12, (e, f) 12 to 18, and	
865	(g, h) 18 to 00 LST during the three days of minimal regional precipitation in the three-day	
866	regional dry-event composite. Zonal and vertical wind changes are in intervals of $0.3 \text{ m s}^{-1}$	
867	and $1.5 \times 10^{-4} \text{ hPa s}^{-1}$ respectively with solid/dashed lines denoting positive/negative	
868	values. The dotted contour denotes the zeroth value. Grey shading in each panel denotes the	
869	minimum surface pressure observed at each longitude in the regional three-day dry event	
870	composite. . . . .	48
871	<b>Fig. 9.</b> Composite-mean, daily-mean changes in relative vorticity (filled, $\text{s}^{-1}$ ) and horizontal wind	
872	(arrows, $\text{m s}^{-1}$ ) at 500 hPa between (a) 00 to 06, (b) 06 to 12, (c) 12 to 18, and (d) 18 to 00	
873	LST during three days of minimal TP precipitation in the dry event composite. Horizontal	
874	wind is regridded to $2^{\circ}$ latitude and longitude for relative vorticity tendencies. The TP is	
875	denoted by a 3000m grey contour in each panel. A horizontal wind scale is shown to the	
876	bottom right of each panel. . . . .	49
877	<b>Fig. 10.</b> (a, b) Mean state (a) temperature (filled, $^{\circ}\text{C}$ ) at 200 hPa and (b) geopotential height (filled,	
878	m) at 850 hPa during day 3.0 of the regional dry event composite. Arrows denote mean state	
879	horizontal winds at (a) 200 and (b) 850 hPa. (c-f) Composite-mean anomalies relative to the	
880	monthly-mean in (c, e) temperature ( $^{\circ}\text{C}$ , filled contours) at 200 hPa and (d, f) geopotential	
881	height (m, filled) at 850 hPa during days (c, d) 3.0, and (e, f) 6.0 of the regional dry event	
882	composite. The TP is denoted by a grey 3000m contour in each panel. Vertical dashed	
883	black lines at 75 and 105° longitude highlight TP's western and eastern boundaries. Orange	
884	horizontal lines at 30 and 40° latitude denotes the meridional range averaged for Hovmöllers	
885	(Fig. 6) and vertical composites (Fig. 8). Grey stippling denotes significance at the 95%	
886	confidence level. Regions filled in white in panels b, d, and f denotes locations where the	
887	surface is above 850 hPa. . . . .	50
888	<b>Fig. 11.</b> Changes in average (a, c, e, g) daily-accumulated precipitation ( $\text{mm day}^{-1}$ ) and (b, d, f, h)	
889	daily-mean temperature ( $^{\circ}\text{C}$ ) in days (a, b) 3.0, (c, d) 4.0, (e, f) 5.0, and (g, h) 6.0 of the	
890	regional three-day dry event composite compared to the boreal summer average. Stippling	

891 denotes a significant change in mean precipitation and temperature at a 95% confidence  
892 level. TP is denoted by a 3000m contour in each panel. . . . . 51

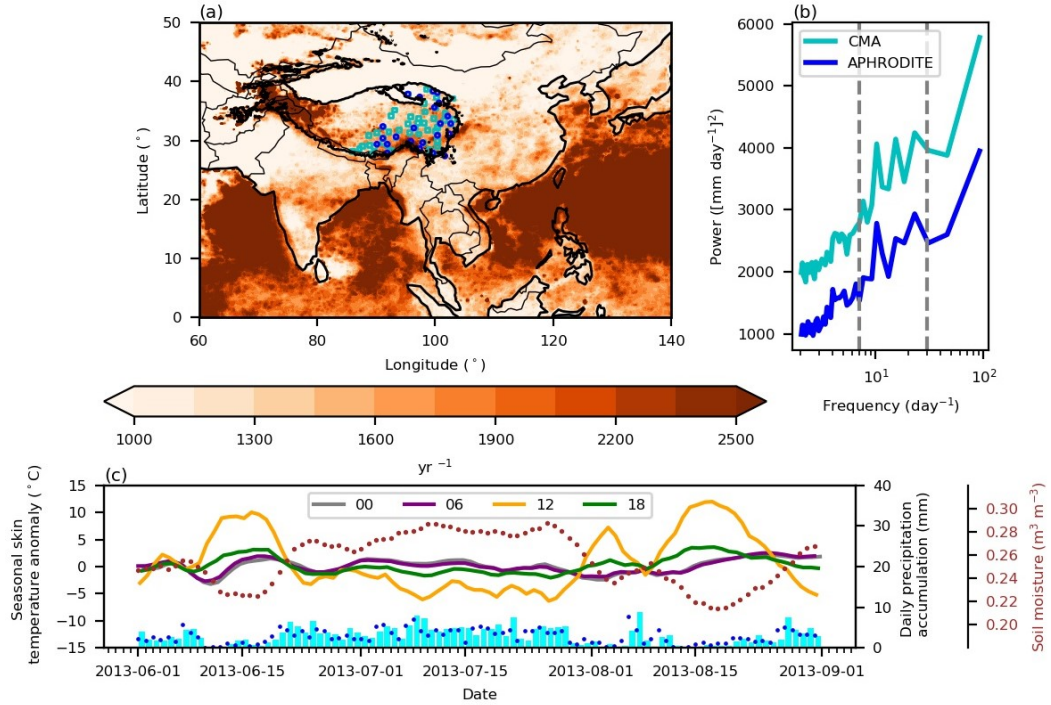


FIG. 1. (a) Annual-mean power associated with 7 to 30 day variability of standardised JJA TRMM precipitation (filled, dimensionless). Cyan squares illustrate the location of weather stations in CMA whilst blue circles denote grid points in APHRODITE with measurements for a minimum of 95% boreal summer days between 1979 and 2015. TP is denoted by a black 3000 m contour. (b) Station-mean, annual-mean power in CMA (cyan) and APHRODITE (blue) JJA daily precipitation accumulations ( $[\text{mm day}^{-1}]^2$ ). Vertical dashed grey lines denote 7 and 30 days. For both (a) and (b) only data between 2000 and 2015 is shown. (c) 5-day running-mean ESA CCI surface soil moisture observations (brown dots;  $\text{m}^3 \text{m}^{-3}$ ) and CMA station-mean skin temperature anomalies ( $^{\circ}\text{C}$ ) at 00 (grey), 06 (purple), 12 (orange), and 18 (green) LST during JJA 2013. Cyan bars and blue dots denote CMA and APHRODITE station-mean daily precipitation accumulations ( $\text{mm day}^{-1}$ ) respectively.

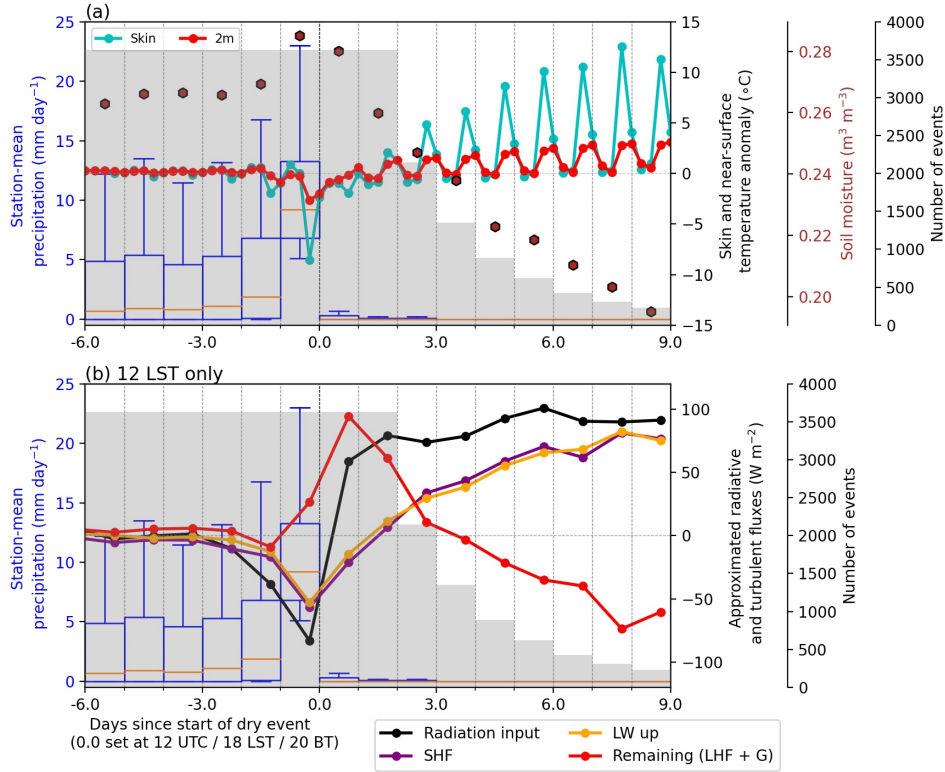


FIG. 2. Mean surface characteristics across all local dry events in boreal summer recorded by the 49 CMA weather stations. (a) Six-hourly anomalous skin (cyan) and near-surface air temperatures (red, °C) along with composite-mean ESA CCI surface soil moisture observations (brown hexagons, m<sup>3</sup> m<sup>-3</sup>). (b) 12 LST SEB components including surface upward longwave radiation ([Eqn. 1], orange), approximated surface SHF ([Eqn. 2], purple), CERES-derived sum of net-downward shortwave and longwave downward radiation (black), and LHF and G (red, W m<sup>-2</sup>). Box-and-whisker plots denote daily precipitation accumulations (mm day<sup>-1</sup>) during a dry event and the preceding six days. The orange line denotes the median; the top and bottom of the box denotes the upper and lower quartiles respectively; and the blue whiskers denote the 10th and 90th percentiles. Grey bars denote the number of events recorded for each dry event length.

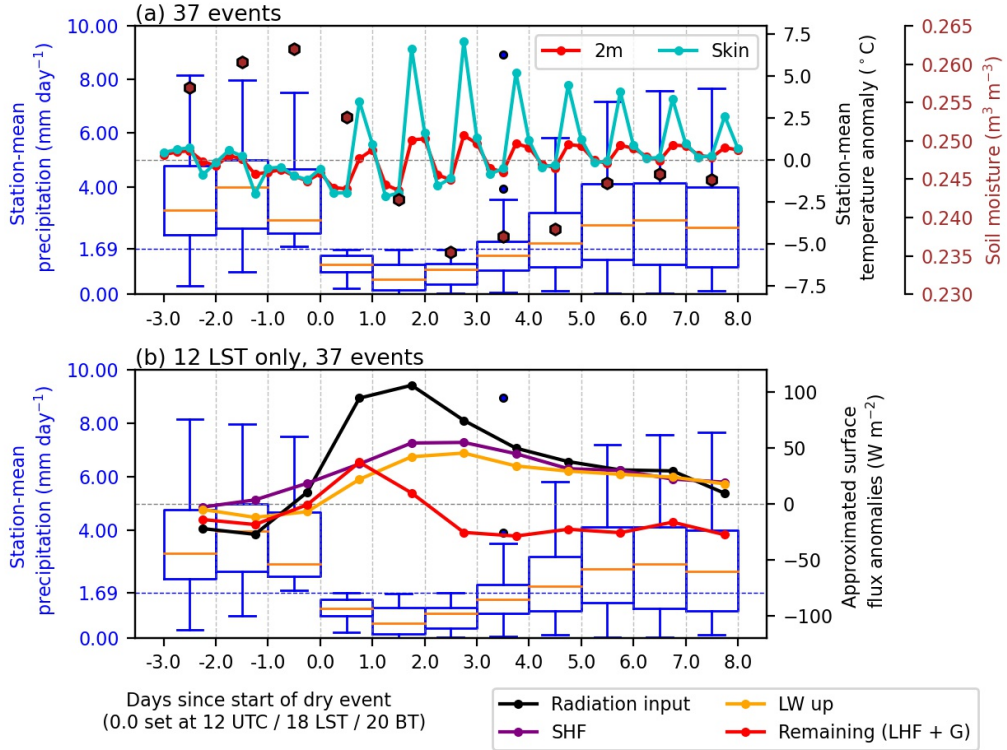


FIG. 3. Anomalous station-mean surface characteristics preceding, during, and after a three-day regional dry event in the CMA dataset. A three-day regional dry event is defined when the station-mean precipitation accumulation is smaller than the twentieth percentile of JJA daily station-mean precipitation, denoted by the blue dashed horizontal line, for three days. (a) Anomalous station-mean near-surface air (red) and skin (cyan, °C) temperatures along with composite-mean ESA CCI surface soil moisture observations (brown hexagons, m<sup>3</sup> m<sup>-3</sup>). (b) Surface upward longwave radiation ([Eqn. 1], orange), approximated surface SHF ([Eqn. 2], purple), CERES-derived sum of net-downward shortwave and longwave downward radiation (black), and LHF and G (red, W m<sup>-2</sup>). Box-and-whisker plots show station-mean daily precipitation accumulations (mm day<sup>-1</sup>). The orange line denotes the median; the top and bottom of the box denotes the upper and lower quartiles; and the blue whiskers denote the 10th and 90th percentiles. Filled blue circles denote outliers in precipitation rates.

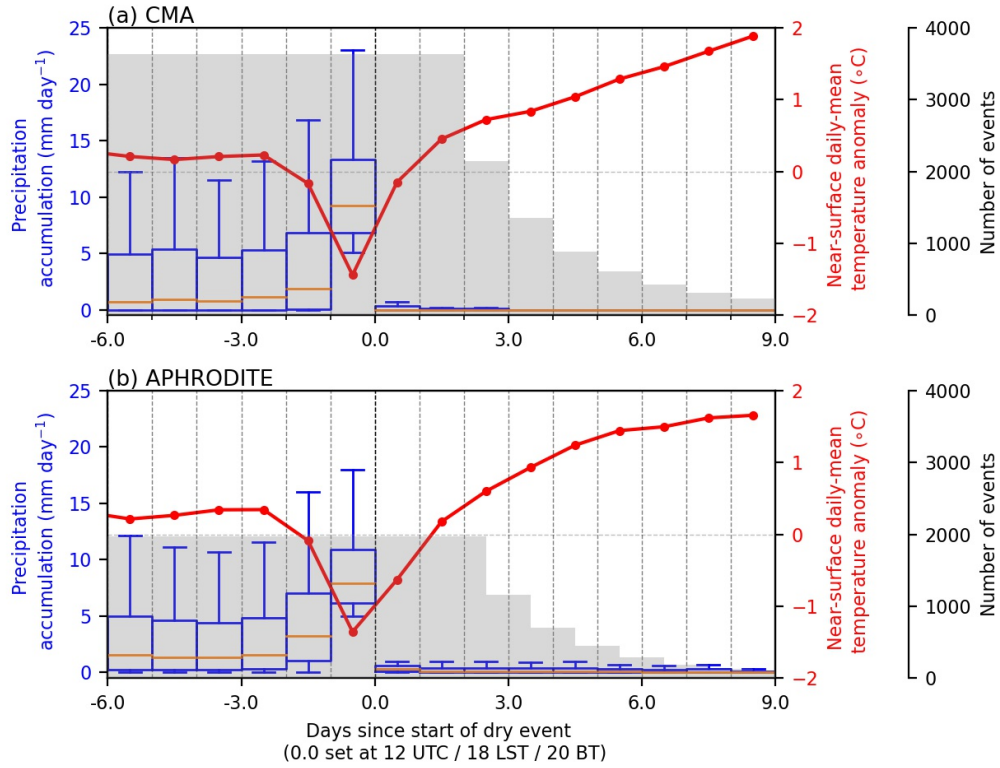
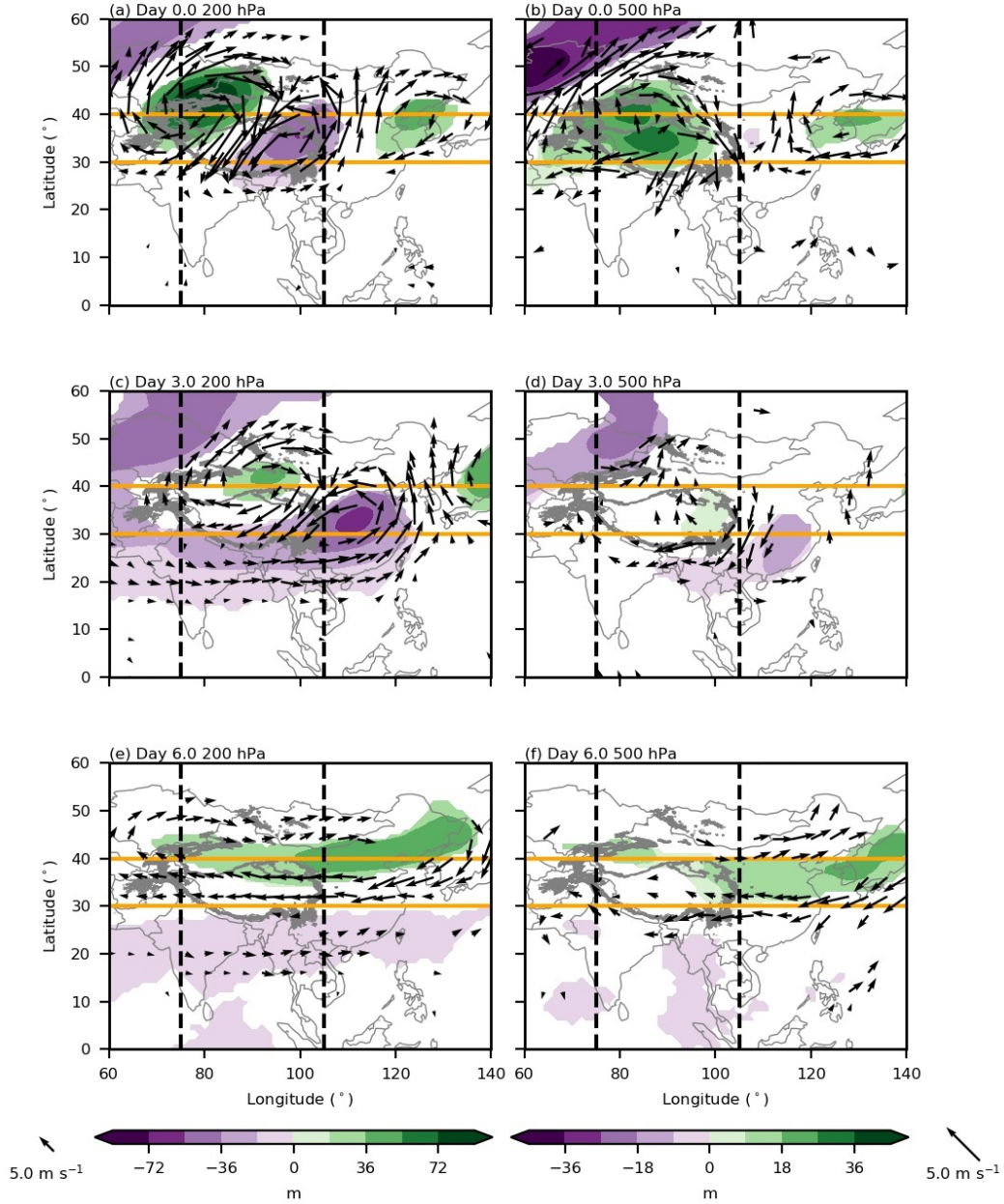
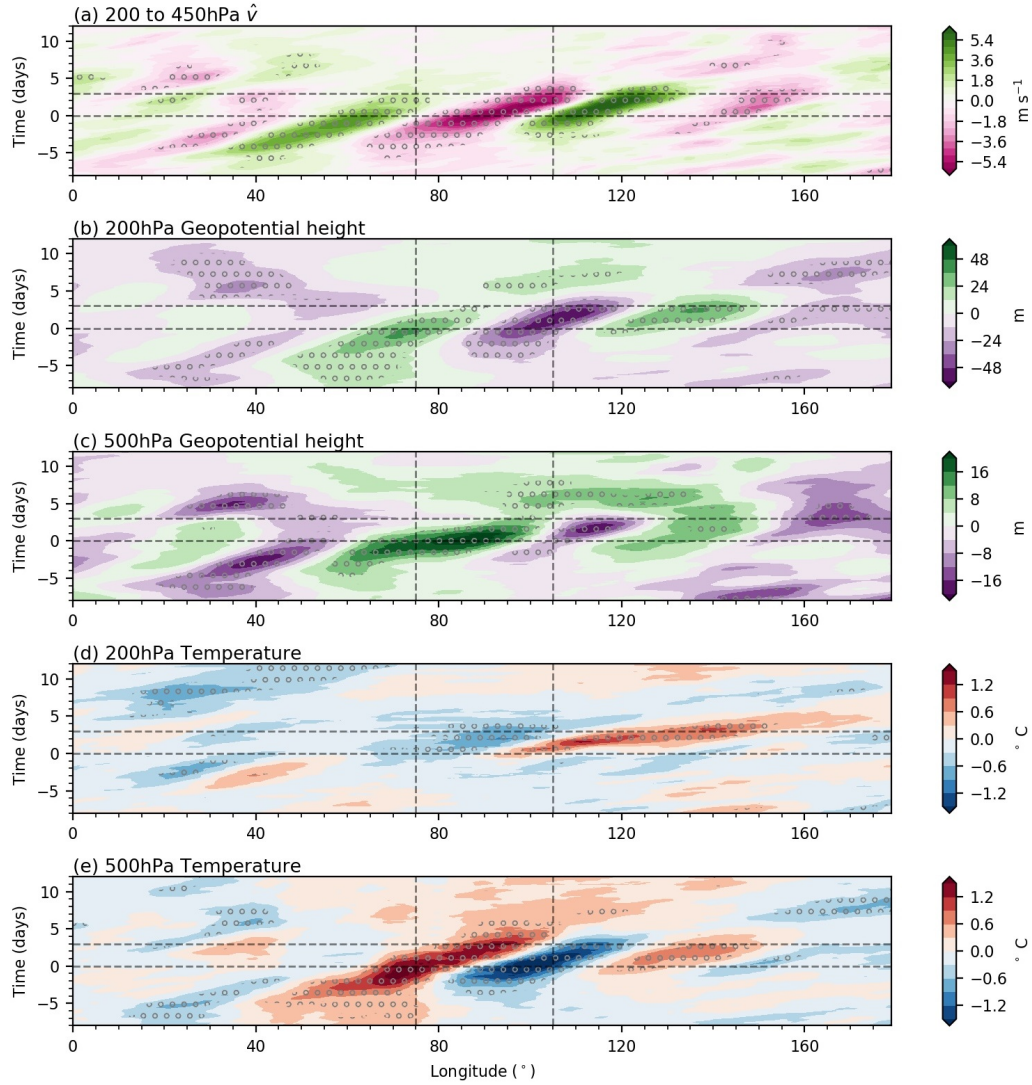


FIG. 4. Anomalous daily-mean near-surface air temperatures ( $^{\circ}\text{C}$ , red line) during localised dry events in (a) CMA and (b) APHRODITE. Box-and-whisker plots denote daily precipitation accumulations ( $\text{mm day}^{-1}$ ) during a dry event and the preceding six days. The orange line denotes the median; the top and bottom of the box denotes the upper and lower quartiles respectively; and the blue whiskers denote the 10th and 90th percentiles. Grey bars denote the number of events recorded for each dry event length.



926 FIG. 5. Composite-mean anomalies relative to the monthly-mean in geopotential height (m, filled contours)  
 927 and horizontal wind ( $\text{m s}^{-1}$ , arrows) during days (a, d) 0.0, (b, e) 3.0, and (c, f) 6.0 of the three-day regional  
 928 dry-spell composite at (a-c) 200 and (d-f) 500 hPa. For each pressure level, different colorbar limits and wind  
 929 arrow sizes are used. The TP is denoted by a grey 3000m contour in each panel. Vertical blue lines at 75 and  
 930 105° longitude highlight TP's western and eastern boundaries. Orange horizontal lines at 30 and 40° latitude  
 931 denotes the meridional range averaged for Hovmöllers (Fig. 6) and vertical composites (Fig. 8). Only data  
 932 significant at the 95% confidence level is shown with wind vectors displayed if significant in either a zonal or  
 933 meridional direction.





934 FIG. 6. Hovmöllers of ERA5 composite-mean, meridional-mean (30 to 40° latitude) anomalies in (a)  
 935 vertically-averaged meridional wind ( $\text{m s}^{-1}$ ) between 200 and 450 hPa, (b, c) geopotential height (m) at (b)  
 936 200 and (c) 500 hPa, and (d, e) temperature ( $^{\circ}\text{C}$ ) at (d) 200 and (e) 500 hPa in the three-day regional dry-event  
 937 composite. Vertical black dashed lines at 75 and 105° longitude highlight TP's western and eastern boundaries  
 938 whilst horizontal dashed lines denote days 0.0 and 3.0 of the regional dry event composite. Stippling denotes  
 939 anomalies significant at the 95% confidence level.



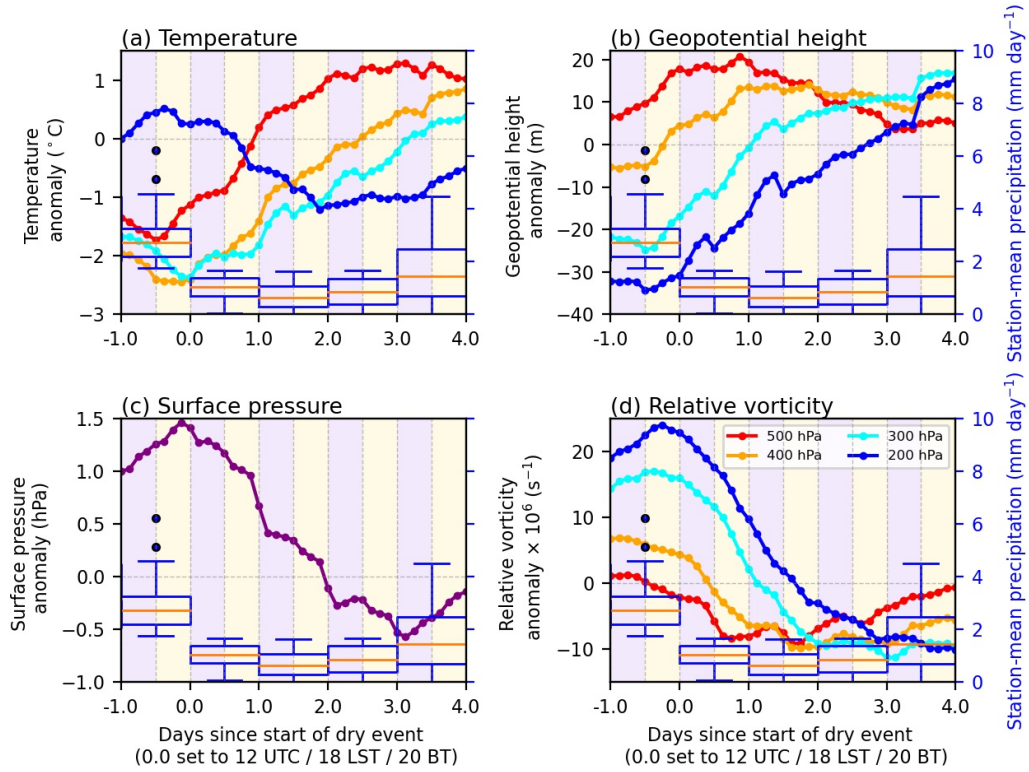


FIG. 7. Composite-mean, regional-mean (30 to 40° latitude, 90 to 100° longitude) anomalous (a) temperature (°C), (b) geopotential height (m), (c) surface pressure (hPa), and (d) relative vorticity ( $\text{s}^{-1}$ ) during the three-day regional dry event composite. For a, b, and d, anomalous values are shown at 500 (red), 400 (orange), 300 (cyan), and 200 (blue) hPa. Box-and-whisker plots in all panels show station-mean daily precipitation accumulations ( $\text{mm day}^{-1}$ ). Upper and lower quartiles are denoted by the top and bottom of boxes; box whiskers denote the 10th and 90th percentiles; and the mean is denoted by an orange line. Background colours in each panel highlight daytime (yellow, 06 to 18 LST) and nighttime (purple, 18 to 06 LST) hours.

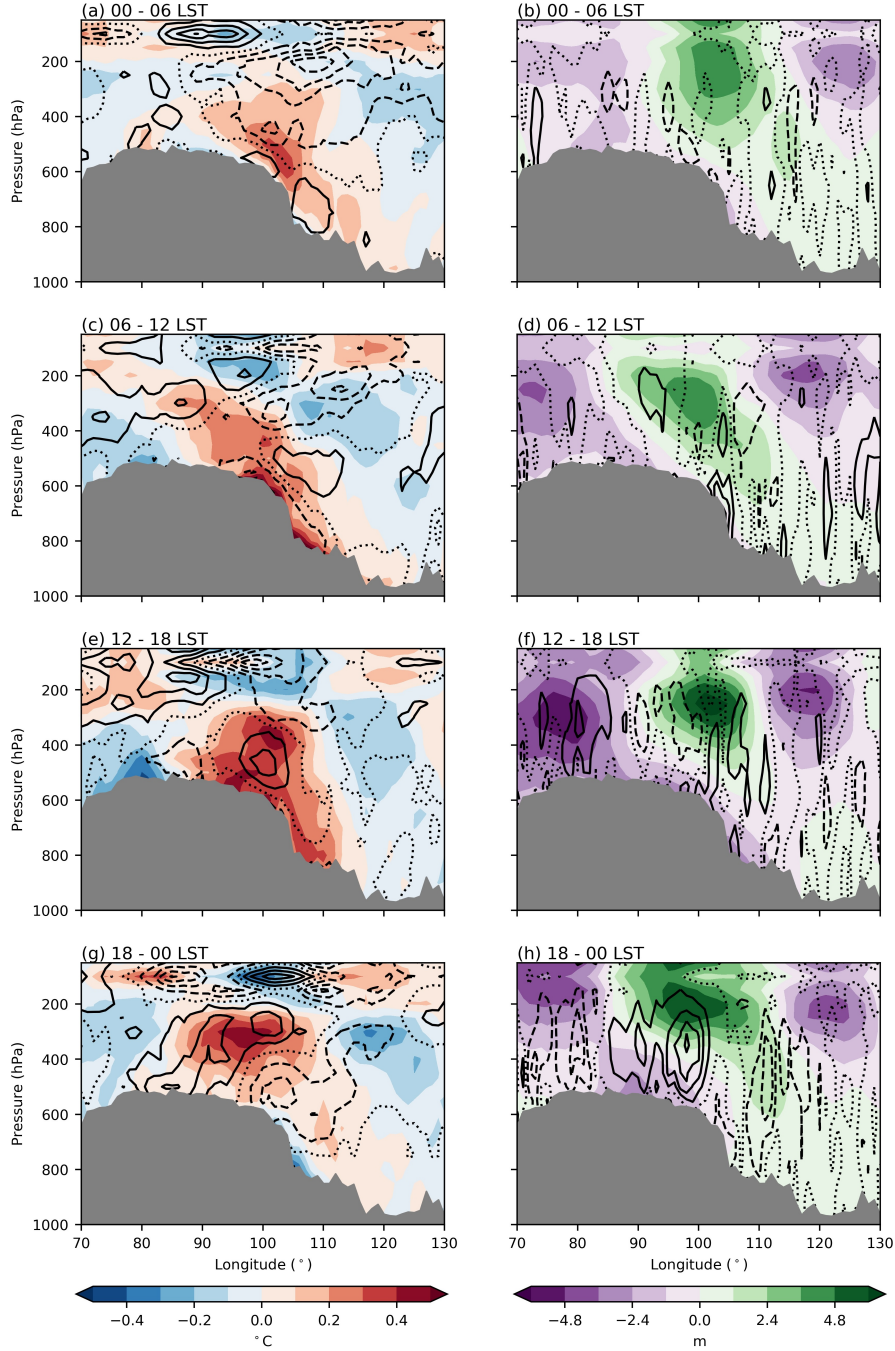


FIG. 8. Changes in composite-mean, daily-mean, meridional-mean (30 to 40° latitude) (a, c, e, g) temperature (filled, °C), zonal wind (lined, m s<sup>-1</sup>), (b, d, f, h) geopotential height (filled, m), and vertical wind (lined, hPa s<sup>-1</sup>) between (a, b) 00 to 06, (c, d) 06 to 12, (e, f) 12 to 18, and (g, h) 18 to 00 LST during the three days of minimal regional precipitation in the three-day regional dry-event composite. Zonal and vertical wind changes are in intervals of 0.3 m s<sup>-1</sup> and  $1.5 \times 10^{-4}$  hPa s<sup>-1</sup> respectively with solid/dashed lines denoting positive/negative values. The dotted contour denotes the zeroth value. Grey shading in each panel denotes the minimum surface pressure observed at each longitude in the regional three-day dry event composite.

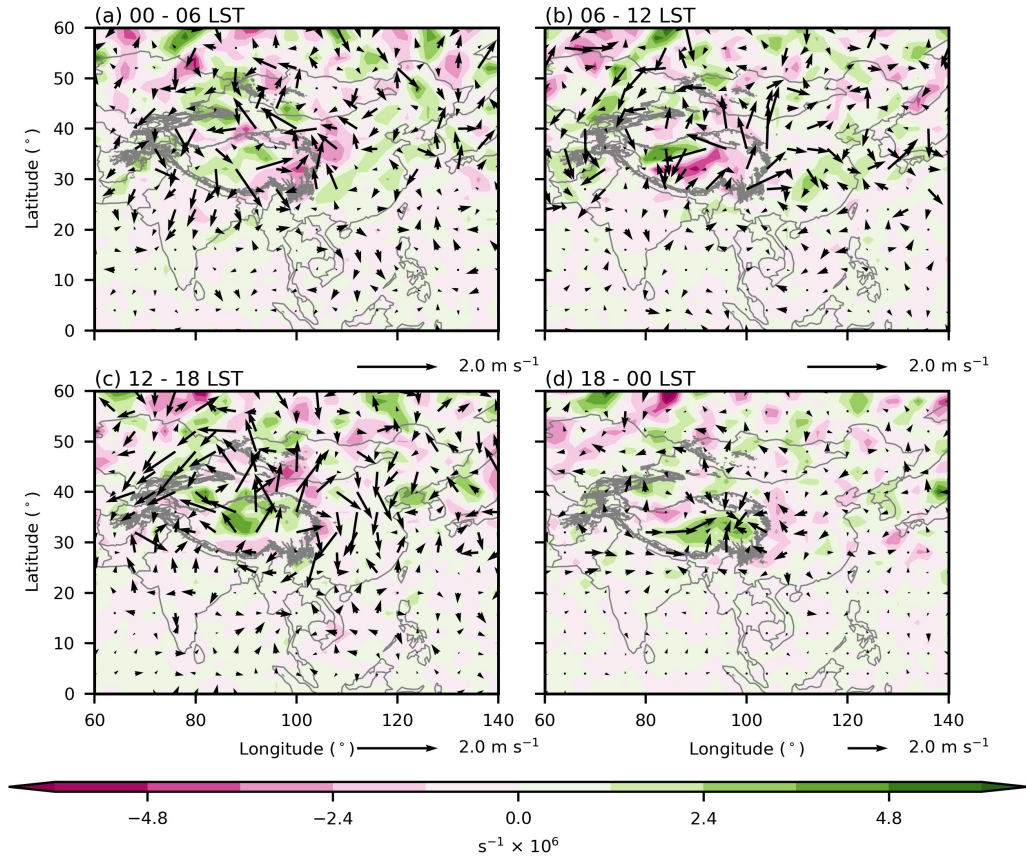


FIG. 9. Composite-mean, daily-mean changes in relative vorticity (filled,  $\text{s}^{-1}$ ) and horizontal wind (arrows,  $\text{m s}^{-1}$ ) at 500 hPa between (a) 00 to 06, (b) 06 to 12, (c) 12 to 18, and (d) 18 to 00 LST during three days of minimal TP precipitation in the dry event composite. Horizontal wind is regrided to  $2^\circ$  latitude and longitude for relative vorticity tendencies. The TP is denoted by a 3000m grey contour in each panel. A horizontal wind scale is shown to the bottom right of each panel.



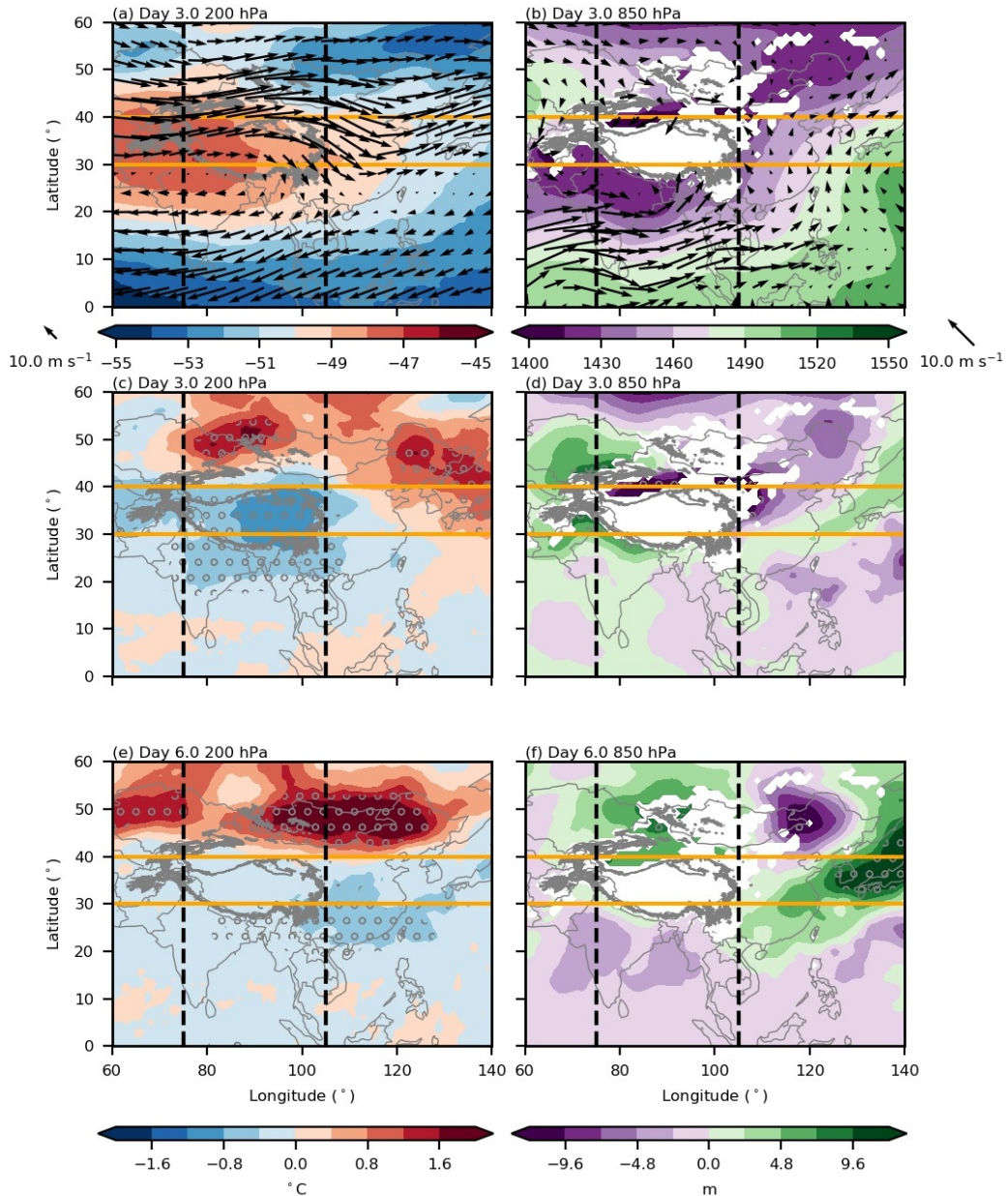


FIG. 10. (a, b) Mean state (a) temperature (filled, °C) at 200 hPa and (b) geopotential height (filled, m) at 850 hPa during day 3.0 of the regional dry event composite. Arrows denote mean state horizontal winds at (a) 200 and (b) 850 hPa. (c-f) Composite-mean anomalies relative to the monthly-mean in (c, e) temperature (°C, filled contours) at 200 hPa and (d, f) geopotential height (m, filled) at 850 hPa during days (c, d) 3.0, and (e, f) 6.0 of the regional dry event composite. The TP is denoted by a grey 3000m contour in each panel. Vertical dashed black lines at 75 and 105° longitude highlight TP's western and eastern boundaries. Orange horizontal lines at 30 and 40° latitude denotes the meridional range averaged for Hovmöllers (Fig. 6) and vertical composites (Fig. 8). Grey stippling denotes significance at the 95% confidence level. Regions filled in white in panels b, d, and f denotes locations where the surface is above 850 hPa.

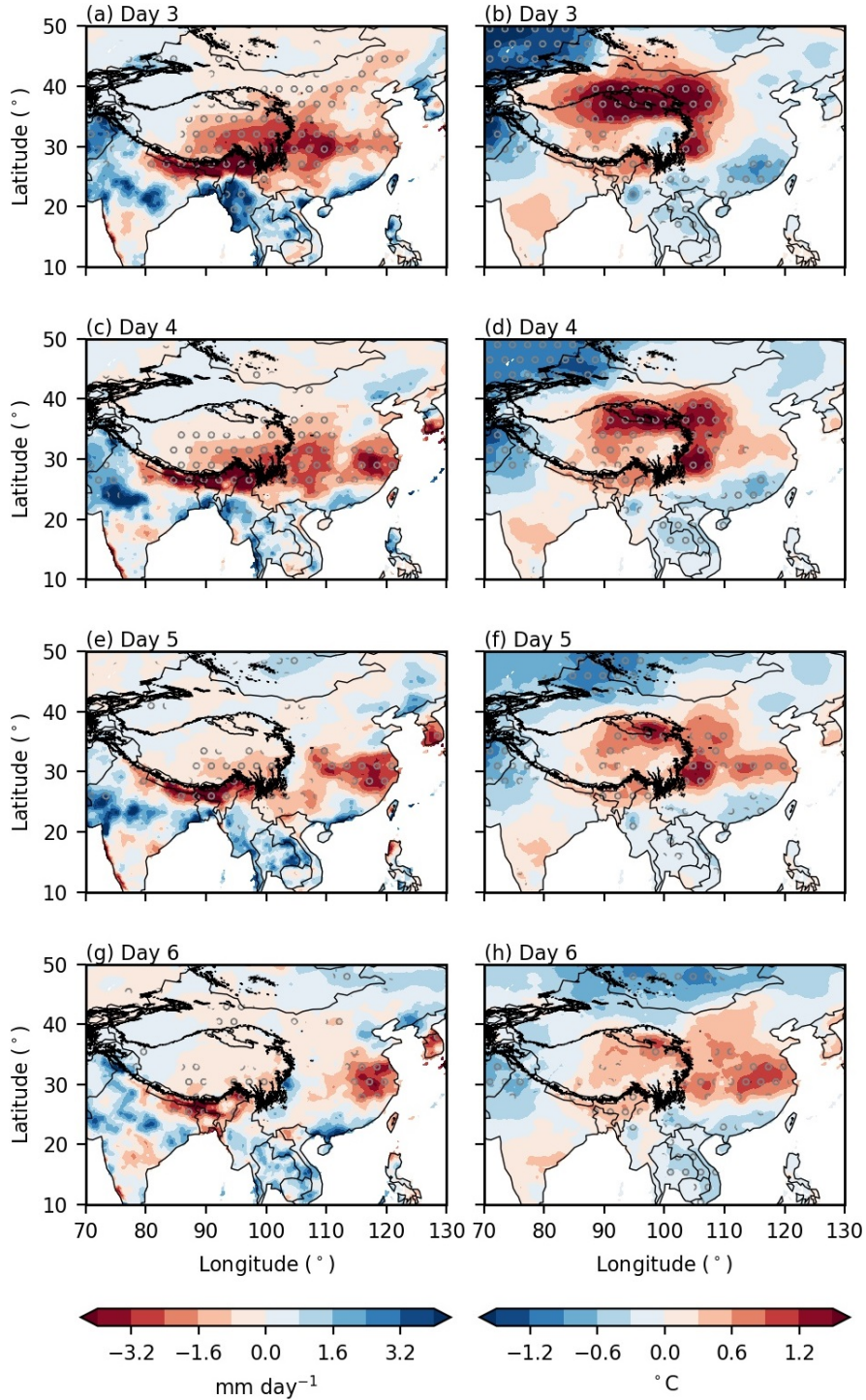


FIG. 11. Changes in average (a, c, e, g) daily-accumulated precipitation ( $\text{mm day}^{-1}$ ) and (b, d, f, h) daily-mean temperature ( $^{\circ}\text{C}$ ) in days (a, b) 3.0, (c, d) 4.0, (e, f) 5.0, and (g, h) 6.0 of the regional three-day dry event composite compared to the boreal summer average. Stippling denotes a significant change in mean precipitation and temperature at a 95% confidence level. TP is denoted by a 3000m contour in each panel.